Icarus 276 (2016) 1–20

Contents lists available at ScienceDirect

Icarus

journal homepage: www.elsevier.com/locate/icarus

Energetics of the martian atmosphere using the Mars Analysis Correction Data Assimilation (MACDA) dataset

Michael Battalio*, Istvan Szunyogh, Mark Lemmon

Department of Atmospheric Science, Texas A&M University, 3510 TAMU, College Station, 77843-3150 TX, United States

ARTICLE INFO

Article history:
Received 10 November 2015
Revised 19 March 2016
Accepted 20 April 2016
Available online 27 April 2016

Keywords:
Atmospheres
dynamics
Mars
atmosphere
Mars
climate

ABSTRACT

The energetics of the atmosphere of the northern hemisphere of Mars during the pre-winter solstice period are explored using the Mars Analysis Correction Data Assimilation (MACDA) dataset (v1.0) and the eddy kinetic energy equation, with the quasi-geostrophic omega equation providing vertical velocities. Traveling waves are typically triggered by geopotential flux convergence. The effect of dust on baroclinic instability is examined by comparing a year with a global-scale dust storm (GDS) to two years without a global-scale dust storm. During the non-GDS years, results agree with that of a previous study using a general circulation model simulation. In the GDS year, waves develop a mixed baroclinic/barotropic growth phase before decaying barotropically. Though the total amount of eddy kinetic energy generated by baroclinic energy conversion is lower during the GDS year, the maximum eddy intensity is not diminished. Instead, the number of intense eddies is reduced by about 50%.

1. Introduction

Traveling waves on Mars are present in both the northern and southern hemispheres, with the maximum amplitude occurring in winter. The northern hemisphere waves are more intense and the focus of the current paper. These waves evolve in both time and space, indicating that the processes behind their creation also depend on space and time.

Interest in traveling waves on Mars stems from a desire to test terrestrial theories on a differing flow regime. More saliently, the ability to forecast weather on Mars grows in importance as further robotic missions are launched to explore the surface, and a reliable forecast must be in place to ensure the safety of any future manned missions. Finally, while it will be shown that global-scale dust storms (GDS) drastically affect baroclinic waves, baroclinic waves themselves can initiate regional dust storms. Thus, the ability to predict and understand these features is of great importance to future missions.

1.1. Waves on Mars

Baroclinic disturbances on Mars have been a subject of intense study in the last few decades. Leovy (1969) first asserted zonal wavenumber 2–4 to be the most unstable baroclinic modes, and Blumsack and Gierasch (1972) found that topography would reduce the growth rates of the most unstable baroclinic modes. The early observational studies, which began with the analysis of observations from the Viking landers (Barnes, 1980; 1981), found that baroclinic instability played a key role in the development of waves in the northern hemisphere. The results confirmed wavenumber 2–4 as prevalent with phase speeds of 10–15 m s^{-1}. Dust was found to dramatically alter the characteristics of traveling waves, warming the midlevels and cooling the surface (Conrath, 1975). Dust was found to reduce the amplitude of waves at low wavenumber (1–2) and increase it at higher wavenumber (3–4) by weakening static stability (Barnes, 1981).

Further insight was gained with the first global climate models (e.g. Pollack et al., 1981; Barnes, 1984), which corroborated the flow favoring wavenumber 2–4. Continued refinement of the models allowed for the exploration of the vertical structure of baroclinic waves (Barnes et al., 1993). The flow at high altitudes was dominated by waves of wavenumber 1–2, with waves of wavenumber 1–4 at the surface. The wavenumber of the dominant waves also increased with optical thickness. Collins et al. (1996) demonstrated that the atmospheric flow flipped between two wavenumber regimes due to diurnal forcing. Hollingsworth and Barnes (1996) anticipated the existence of storm tracks in the northern hemisphere due to the strong zonal inhomogeneity of the surface topography. Using the NASA Ames Mars Global Circulation Model (MGCM) simulation, Hollingsworth et al. (1996) determined that storms would be preferred in the lowland Planitias and would

* Corresponding author. Tel.: +1 6014159805.
E-mail address: michael@battalio.com, battalio@tamu.edu, mbattalio@gmail.com (M. Battalio).

http://dx.doi.org/10.1016/j.icarus.2016.04.028
0019-1035/

be guided by a topographically forced, wavenumber-two stationary wave.

Traveling waves have been identified using observations from Mars Global Surveyor. Hinson and Wilson (2002) focused on the southern hemisphere and found such waves at wavenumber 3. Wilson et al. (2002) identified wavenumber 1 traveling waves in the northern hemisphere during winter in both Thermal Emission Spectrometer (TES) observations and Geophysical Fluid Dynamics Laboratory (GFDL) MGCM simulations. Banfield et al. (2004, 2003) analyzed forced and traveling waves in TES data, concluding that wavenumber 1 wave had the highest amplitude. Wavenumber 2 and 3 waves prevailed during fall and spring with a lull around the winter solstice.

Subsequent work described the relationship between global-scale dust storms and traveling waves. Basu et al. (2006) defined two categories of GDS: storms that begin in the Hellas basin and northern hemisphere storms initiated by traveling waves. The superposition of waves provided a sufficiently large surface wind stress to trigger dust lifting. “Flushing” dust storms that transport dust from the polar ice cap to the lower latitudes were primarily baroclinic fronts associated with waves of period 2–3 Sol and wavenumber 3 (Wang et al., 2005). Hinson and Wang (2010) defined three key factors that influenced the flushing storms: baroclinic mode transitions, storm zones that strongly modify the zonal amplitude of baroclinic eddies, and stationary waves.

Work has been done on the variation of baroclinic waves induced by the seasonal variation of dust opacity (Kuroda et al., 2007). In northern hemisphere autumn, waves weaken as solstice approaches due to the tilt of the polar front becoming poleward with height from equator-ward with height. Increased dust loading was found to modify baroclinic activity by intensifying the westerly jet due to strengthening of the meridional temperature gradient in the mid-levels. This stabilizes the jet stream to low-wavenumber disturbances. Lewis et al. (2016) further elucidated the solsticial pause in baroclinic wave activity, which occurs within $L_s = 240$–$300°$ period in the northern hemisphere, using the MACDA reanalysis, and a related paper from Mulholland et al. (2016) used the UK MGCM to find that water ice clouds modifying the Eady growth rate of baroclinic waves along with zonally asymmetric topography were the most likely cause. Energy conversion was explored by Greybush et al. (2013), who found that baroclinic energy conversion took place near the surface, and baroclinic and barotropic conversions were important in the westerly jets aloft. Additionally, topography played a key role in the development of storm tracks due to lee cyclogenesis. A recent study by Mooring and Wilson (2015) investigated the spatial structure and propagation of transient eddies in the MACDA reanalysis. They found a pattern of about wavenumber 3 on either side of the solstitial pause in the northern hemisphere with eddy kinetic energy maxima prevalent in areas of low topography.

1.2. Local energetics

The nature of baroclinic instability and its role in the development of synoptic-scale waves have been well understood in the terrestrial atmosphere for several decades. The models of Charney (1947) and Eady (1949) established baroclinic instability as the prime driver of mid-latitude, synoptic-scale atmospheric dynamics. Since the first formulation of the theory of baroclinic instability, much effort has been expended in investigating the initiation and development of waves caused by baroclinic energy conversion. Traveling waves in the midlatitudes have been found to grow baroclinically and decay barotropically (Simmons and Hoskins, 1979; 1978; 1980). The leading edge of an initially localized disturbance propagates as a packet of traveling waves at the associated group velocity, while the trailing end stabilizes with no further upstream motion (Swanson and Pierrehumbert, 1994).

The establishment of the local energetics method began with the work of Orlanski and Katzfey (1991), who studied the evolution of cyclones in terms of a local kinetic energy budget. In particular, they examined a common form of cyclogenesis in which storms are triggered by upper tropospheric wave packets through the convergence of geopotential height fluxes, grow by baroclinic conversion of potential energy to eddy kinetic energy, transport kinetic energy downstream via the background flow and via geopotential flux divergence, and lose kinetic energy to the background flow through barotropic energy conversion. In principle, baroclinic energy conversion can occur spontaneously, but in practice, it is usually triggered by upper-tropospheric traveling waves. A follow-up study (Orlanski and Sheldon, 1993) defined the process as downstream baroclinic development, as the convergence of geopotential fluxes was immediately followed by baroclinic energy conversion. Downstream baroclinic development was explored in an idealized situation by Chang and Orlanski (1993). They found that baroclinic energy conversion was correlated with maximum baroclinicity, but geopotential flux convergence acted to maintain eddies downstream of the unstable baroclinic regions, extending the storm tracks downstream into weakly unstable areas. Chang (1993) provided observational evidence of the role of geopotential fluxes in the Pacific storm track.

Orlanski and Sheldon (1995) applied local energetics to cyclone development to create a model of downstream baroclinic evolution. In this conceptual model, an eddy kinetic energy (EKE) center disperses energy downstream through geopotential flux divergence, generating a new EKE center. Next, the second EKE center grows baroclinically as geopotential fluxes begin to diverge. Lastly, the second EKE center decays via geopotential fluxes and barotropic conversion. The group velocity of the resulting packets of traveling waves is greater than the phase speed of the individual troughs and ridges, so troughs grow on the downstream side of the wave packet and decay on the upstream side. Downstream development often leads to development at the surface (Chang, 2000). Decker and Martin (2005) showed that the location of the development within the downstream expanding packet can determine the lifetime of the cyclone. The further downstream within a wave packet that an EKE center develops, the longer the lifetime of a cyclone.

We base our work on that of Kavulich et al. (2013) (hereafter K13), who found by analyzing simulations with the GFDL MGCM that the main concepts of storm track dynamics also apply to the northern hemisphere cold season circulation of the mid-latitudes of Mars. They found that the main role of baroclinic energy conversion is to maintain already existing downstream propagating packets of waves rather than starting a new chain of baroclinic developments. The role of barotropic energy conversion in the downstream propagating packet depends on the local topography. In a channel north of the Tharsis Plateau, it enhances the kinetic energy of the wave packet and extends the region where eddies can exist south, while elsewhere it serves as a sink of kinetic energy.

We apply the eddy kinetic energy equation (Orlanski and Katzfey, 1991) to three years of the Mars Analysis Correction Data Assimilation (MACDA) global reanalyses, for the $L_s = 200$–$230°$ period. We compare the development and decay of baroclinic waves to that observed in previous work, both on Mars and on Earth. In particular, our focus is on the impact of the Mars Year (MY) 25 GDS on baroclinic activity compared to the varying dustiness of MY 24 and 26 and inter-annual variability of the flow. The paper is organized as follows: Section 2 describes the dataset used and the average flow properties. Section 3 discusses our implementation of the eddy kinetic energy equation. Section 4 investigates the time-mean energetic properties of the flow. Section 5 follows the evolution of two prototypical waves: one in a non-GDS year (MY 24) and one in a GDS year. Section 6 compares the intensity of the eddy kinetic energy generation mechanisms between the investigated years. Section 7 summarizes our main conclusions.

2. MACDA

MACDA (v1.0) (Montabone et al., 2014) is a reanalysis of assimilated vertical temperature profile retrievals and column dust optical depth retrievals from $L_s = 141^\circ$ in Mars Year 24 to $L_s = 86^\circ$ in MY 27 (February 1999 to August 2004). The temperature profiles were retrieved from radiance observations by the TES instrument that was flown onboard Mars Global Surveyor in a Sun-synchronous polar orbit. The observations provide information about the vertical temperature profile up to 40 km twice a day at approximately 2 a.m. and 2 p.m. local time and total atmospheric column dust optical depth every sol around 2 p.m. local time for the tropics and midlatitudes. Retrievals were assimilated into the UK version of the LMD-UK MGCM (Montabone et al., 2014), which shares the physical parameterizations with the LMD MGCM (Forget et al., 1999), using an assimilation scheme described by Montabone et al. (2006) and Lewis et al. (2007). The dataset is made available publicly on a 5° by 5° resolution, latitude-longitude grid with 25 terrain-following sigma levels every two Mars hours. We note the caveat that the MACDA has been shown to have some bias in the TES retrieval scheme during the MY 25 GDS (Montabone et al., 2006), but that the MACDA reanalysis is an improvement on free runs of the UK MGCM as it does contain the well observed solstitial pause in eddy activity in each Mars year (Lewis et al., 2016; Mooring and Wilson, 2015).

The MACDA dataset has been used in several studies to describe the nature of the martian atmosphere. Mitchell et al. (2014) compared polar vortices on Mars to those of Earth, Hurley et al. (2014) used MACDA temperature retrievals to constrain model CO_2 condensation levels, Lovejoy et al. (2014) used MACDA for verification of winds of MGCM simulations, and Wang and Mitchell (2014) used MACDA to diagnose the Rossby and Froude numbers in a study of atmospheric superrotation. The MACDA reanalysis has become popular to investigate traveling waves in martian atmosphere, as in Lewis et al. (2016) and Mooring and Wilson (2015). The Lorenz energy budget has also been studied over diurnal, seasonal, and annual time-scales using MACDA (Tabataba-vakili et al., 2015).

2.1. Dust storms

The global-scale dust storm of MY 25 was initiated in the southern hemisphere by a series of local storms forced by the thermal contrasts between the retreating ice cap and bare ground of Hellas basin. It was a merging development in the classification of Wang and Richardson (2015). Just after the spring equinox ($L_s = 177^\circ$), a large storm entered the Hellas Basin causing a rapid increase in the amount of surface obscured by dust. By $L_s = 185^\circ$, the dust spread rapidly east toward the Tharsis Plateau, where additional dust lifting areas developed, and the dust storm fully encircled the equatorial and mid-latitude regions by $L_s = 195^\circ$. Lifting continued until $L_s = 212^\circ$, at which time the dust was uniformly distributed (Strausberg, 2005). Dust slowly precipitated out to seasonal levels by $L_s = 304^\circ$ (Cantor, 2007). Citing the large diurnal variation in temperature and modified latitudinal temperature structure, Smith (2002) noted that the dynamics of the atmosphere were changed by the dust storm. The northern hemisphere polar vortex served as a boundary to the dust storm: south of the polar vortex, vertical temperatures increased by over 40 K (Smith, 2002) (see Section 2.2.1).

The strength of the GDS is juxtaposed to the non-GDS years in Fig. 1, which shows the optical depth for each Mars year in the MACDA dataset. The general trend of slowly increasing dust approaching northern hemisphere winter is similar in all years up to $L_s = 177^\circ$, then rapid column optical thickening occurs in MY 25, while the opacities continue to slowly increase in MY 24 and 26. The dust storm rapidly expands out to 40°N but then northward growth slows, only reaching 55°N by $L_s = 230^\circ$.

Beyond the main GDS of MY 25, MY 24 and 26 each had regional dust storms during $L_s = 200–230^\circ$: during MY 24, a storm occurred from $L_s = 220–230^\circ$ in Acidalia Planitia and $L_s = 202–205^\circ$ also in Acidalia (Cantor et al., 2001; Wang et al., 2005); while in MY 26, a storm traveled north to south through Utopia Planitia during $L_s = 205–219^\circ$ (Cantor, 2007; Wang and Richardson, 2015). Montabone et al. (2005) compares the evolution of total dust optical depth in these regional dust storms to the GDS in MY 25 in their Fig. 3, which shows the northern hemisphere has much lower optical depth than the southern hemisphere in general, particularly in MY 25. Returning to MACDA in Fig. 1, it can be seen that MY 24 has smaller column optical depth than MY 26. The total average optical depth between 57.5°N and 82.5°N over the $L_s = 220–230^\circ$ period is 0.53, 1.15, and 0.74 for MY 24, 25, and 26, respectively. In several ways, MY 26 is more similar to MY 25 than MY 24 as a result of the increased dustiness from regional storms, and these regional storms temporarily modified the local energetics as they traveled and dissipated.

2.2. Average flow properties

2.2.1. Zonal-mean temperature and winds

The zonal mean temperature fields at $L_s = 200^\circ$ (Fig. 2, top row) and 230° (Fig. 2, second row) are shown for MY 24 (left column), MY 25 (middle column), and MY 26 (right column). The key feature of the zonal-mean temperature fields is the meridional temperature gradient located near 60°N. At the initial time, MY 24 and 26 have a structure in their polar front that supports baroclinic instability with a tilt of the gradient away from the pole with increasing height, agreeing with K13 and the studies based on TES observations. In MY 25, the tilt is in the opposite direction, which is unfavorable for baroclinic instability at lower levels.

Also evident at $L_s = 200^\circ$ is the effect of dust on the lower latitudes in MY 25. The 100–10 Pa layer between 30°N and 30°S is approximately 40 K warmer, and the surface is approximately 10 K cooler on average. This is a result of the higher optical thickness absorbing solar radiation in the upper levels at the expense of surface. Increased dust also affects the meridional circulation (e.g. Montabone et al., 2005, Fig. 7) by strengthening the Hadley cells, which explains the polar warming in the mid-levels via adiabatic processes and the maintenance of the strong meridional temperature gradient. At the later time of $L_s = 230^\circ$, all years display a poleward tilt to the polar front, inhibiting baroclinic instability. Kuroda et al. (2007) found a similar suppression of baroclinic activity due to the increased poleward tilt at $L_s = 280–300^\circ$. The meridional temperature gradient decreases at the surface, limiting the sensitivity of the flow to baroclinic instability as the winter solstice approaches. The temperature of the upper levels in MY 25 still indicates increased warming over the clear years, but the lower level cooling disappears.

All three Mars years show an intensifying westerly jet from $L_s = 200^\circ$ (Fig. 2, third row) to 230° (Fig. 2, bottom row) in the northern hemisphere and a weakening jet in the southern hemisphere as Mars approaches northern hemisphere winter. The stronger westerly jet is consistent with the increased meridional temperature gradient through geostrophic balance. The increased vertical shear shifts the most unstable wavenumber to smaller values (Kuroda et al., 2007). The subtropical jet increases in strength

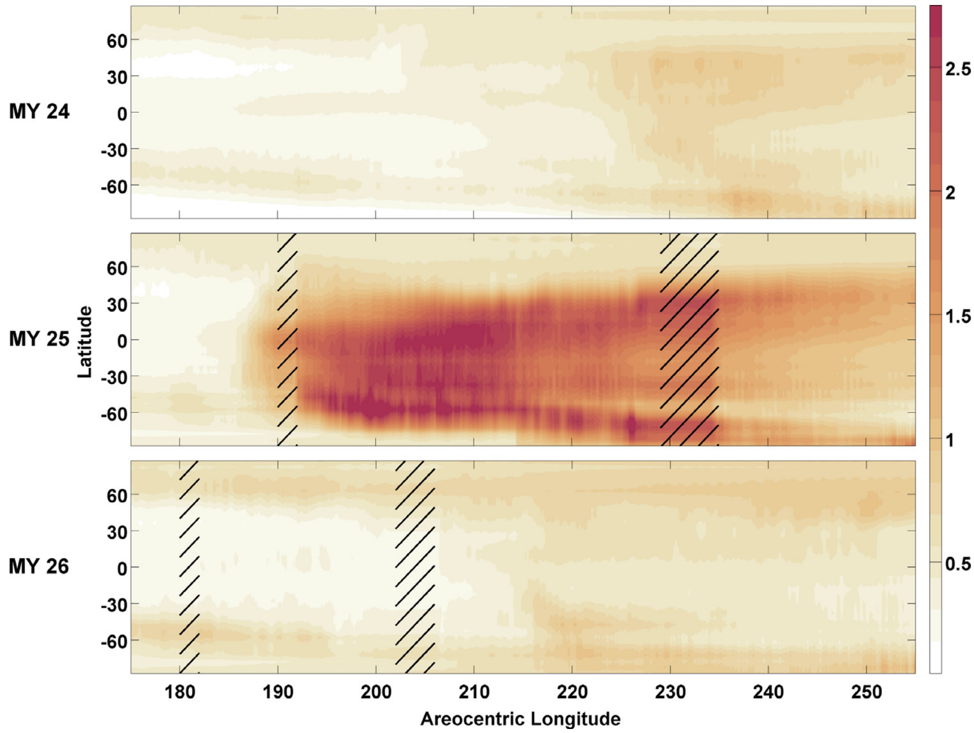

Fig. 1. Column optical depth in the visible wavelength range for L_s = 175–255° for MY 24 (top), MY 25 (middle), and MY 26 (bottom) from the MACDA dataset. Hatching indicates times of areocentric longitude greater than one degree, when TES retrievals were unavailable, and the analyses are based on a freely running model unconstrained by observations.

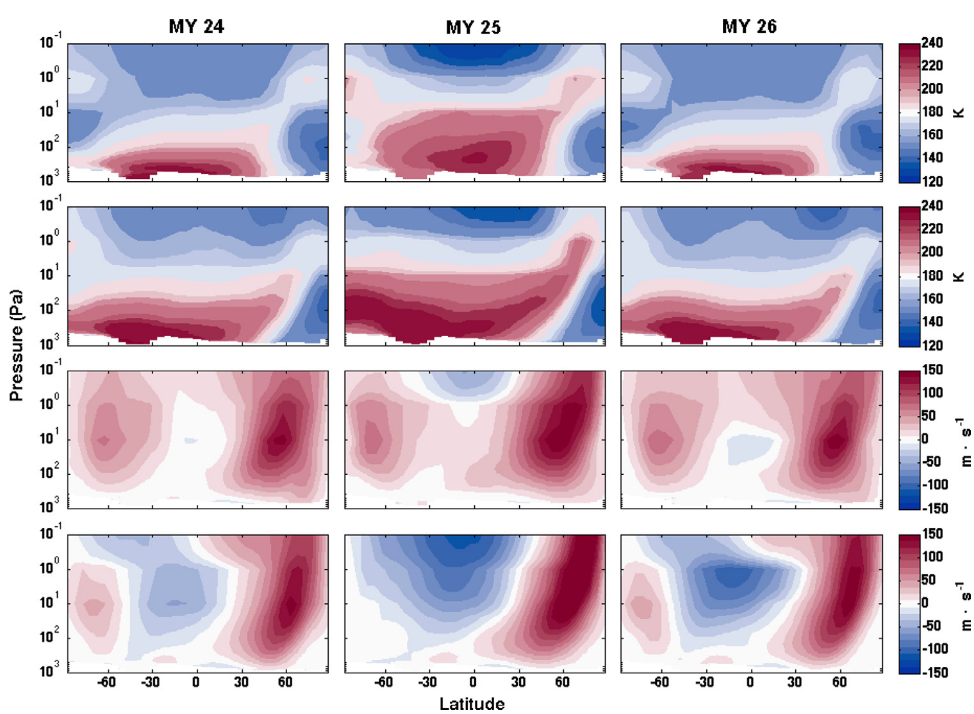

Fig. 2. The zonal mean temperature field for L_s = 200° (top row) and L_s = 230° (second row), and the mean zonal wind field for L_s = 200° (third row) and L_s = 230° (bottom row) for MY 24 (left), MY 25 (middle), and MY 26 (right).

as the Hadley circulation strengthens. The stronger subtropical jet in MY 25 is due to a positive feedback mechanism between the Hadley circulation and dust lifting centers. Haberle et al. (1993) and Murphy et al. (1995) showed that as dust is entrained into the Hadley circulation, the circulation strengthens, intensifying the subtropical jet. The stronger jet increases the likeliness of dust lifting via enhanced surface wind stress, possibly further increasing the optical depth (Basu et al., 2006).

2.2.2. Eddy components

To remove the diurnal signal from variables, a Hamming window digital filter was used to remove the frequency band

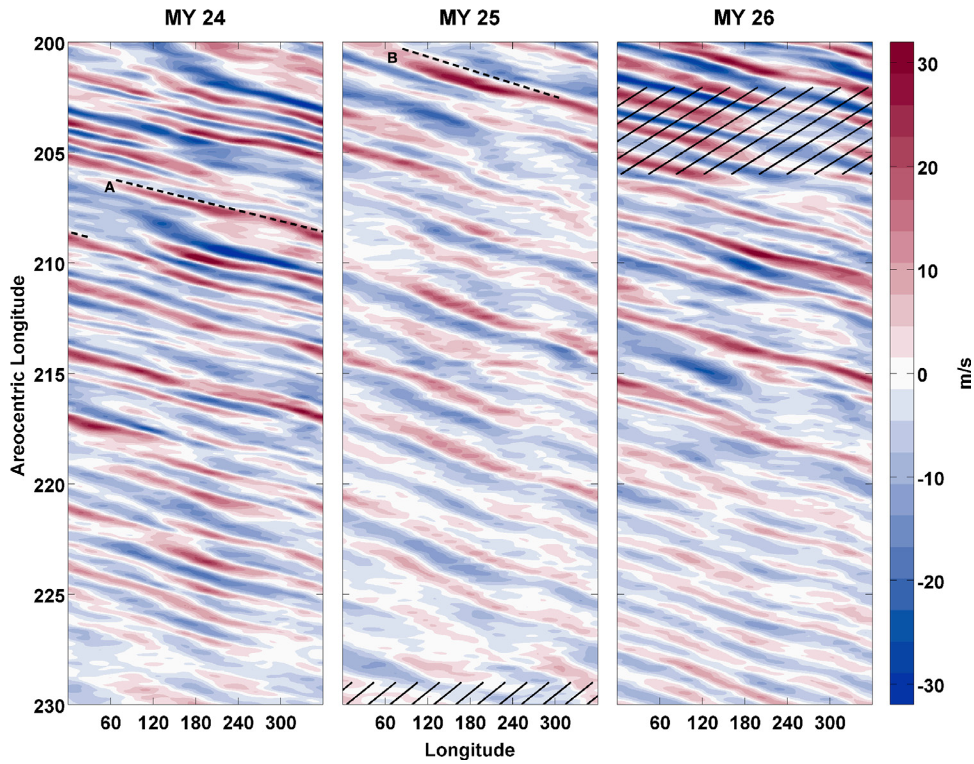

Fig. 3. Hovmöller diagram for the eddy component of the meridional wind field at 300 Pa for L_s = 200–230° in the 57.5–82.5°N band. Shown are MY 24 (left), MY 25 (middle), and MY 26 (right). Lines A and B refer to the location of storms discussed in Sections 5.1 and 5.2. Hatching indicates times of areocentric longitude greater than one degree, when TES retrievals were unavailable, and the analyses are based on a freely running model unconstrained by observations.

0.95–1.05 Sol^{-1} and frequencies higher than 1.82 Sol^{-1} from each variable of the MACDA dataset as in K13. Filtering in this way removed the diurnal and semidiurnal tides, respectively; the value 1.82 Sol^{-1} was specifically chosen to remove signals from the time step immediately preceding local noon to prevent any semidiurnal tide signal as $10/12 = 0.833$. To obtain the mean state, a 30-Sol running mean was calculated for all variables. A 30-Sol mean was chosen as it was sufficiently long to capture the seasonal signal while also removing any signal from the baroclinic waves themselves. The filtered variables will be distinguished from the averages with a superscribed prime.

A Hovmöller diagram (Fig. 3) of the eddy component of the meridional wind in the 57.5–82.5°N band shows the variations in the propagation of transient waves in the westerly jet at 300 Pa. Waves primarily have a wavenumber between 2 and 3 with periods between 4 and 5 Sols. Waves occur throughout the study period in MY 24 and MY 26; however, waves exhibit reduced amplitude as time advances. MY 24 displays a decreasing transient wave amplitude after $L_s = 225^\circ$, and MY 26 shows decaying amplitude beginning after $L_s = 215^\circ$ with the primary contribution from flushing dust storms in the eastern hemisphere beforehand. This reduction in wave activity at the end of the study period is reflective of the reversed tilt of the polar front toward $L_s = 230^\circ$ (Fig. 2) and the regional dust storms occurring at this time in each year, particularly MY 26. In MY 25, amplitudes are substantially reduced due to the GDS limiting baroclinic development. The primary growth regions of the waves also differ between years. The MY 24 and MY 25 waves increase their amplitude near 180°E, while the MY 26 waves grow upstream near 60°E.

3. Eddy kinetic energy

The eddy kinetic energy equation (Orlanski and Katzfey, 1991) is given as

$$\frac{\partial}{\partial t}\langle K_e\rangle = \overbrace{-\langle \nabla\cdot \mathbf{v}K_e\rangle}^{1}\overbrace{-\langle\nabla\cdot\mathbf{v}'\phi'\rangle}^{2} \overbrace{-\langle\omega'\alpha'\rangle}^{3}\overbrace{-\langle \mathbf{v}'\cdot(\mathbf{v}_3'\cdot\nabla_3)\mathbf{v_m} - \mathbf{v}'\cdot\overline{(\mathbf{v}_3'\cdot\nabla_3)\mathbf{v}'}\rangle}^{4} \overbrace{-[\omega'K_e]_s+[\omega'K_e]_t}^{5}\overbrace{-[\omega'\phi']_s+[\omega'\phi']_t}^{6}\overbrace{+\langle(Residue)\rangle}^{7}, \quad (1)$$

where the kinetic energy per unit mass is defined as $K_e = \frac{1}{2}(u'^2 + v'^2)$, ϕ is the geopotential height, $\alpha = 1/\rho$ is the specific density, $\mathbf{v}' = (u', v')$, and $\mathbf{v}_3' = (u', v', \omega')$. Primed variables indicate the eddy components, and $\mathbf{v_m}$ is the time-mean flow. The overbar is a time average, angle brackets denote a mass-weighted vertical average where pressure is the vertical coordinate, and square brackets indicate surface integrals over the surface (s) or top of the atmosphere (t).

Each term on the right-hand side of Eq. (1) describes a process that can change the eddy kinetic energy. Term 1 describes eddy kinetic energy advection by the total flow. Term 2 is the ageostrophic, geopotential flux convergence (GFC) term. When this term is positive, height fluxes are converging, the potential energy of the eddy decreases, and EKE increases. It must be noted that terms 1 and 2 are transport terms, as their integral across the entire surface is zero; thus, they cannot be an ultimate source or sink of EKE.

Term 3 is the baroclinic energy conversion (BCEC) term. When BCEC is positive, EKE is generated from the eddy available potential energy. Term 4 is the barotropic energy conversion (BTEC) term and is positive when kinetic energy is transferred from the background flow and negative when kinetic energy is transferred to the basic flow.

Term 5 describes vertical fluxes of EKE and can be considered the vertical part of the advection term. It is neglected in our calculations because it is approximately two orders of magnitude smaller than the other terms. Term 6 is the vertical potential energy flux at the top and bottom of the atmosphere and can be understood to be the vertical contribution from the GFC term. We consider 1 Pa to be the top of the atmosphere as the top three sigma levels in the MACDA MGCM are sponge levels and are consequently neglected. In the terrestrial atmosphere, term 6 is usually small and can be neglected, but it was found that for the martian atmosphere, term 6 was only one order of magnitude smaller than the other terms. Throughout the rest of the study, references to the GFC term will refer to the sum of terms 1 and 2, as $-[\omega'\phi']_s + [\omega'\phi']_t = \frac{\partial(\omega'\phi')}{\partial p}$ so that

$$-\overline{\nabla_3 \cdot \mathbf{v}_3'\phi'} = -\overline{\nabla \cdot \mathbf{v}'\phi'} - \overline{\frac{\partial(\omega'\phi')}{\partial p}}. \tag{2}$$

It should also be noted that ideally the surface integral $-[\omega'\phi']_s$ is zero as the boundary condition for vertical motion in a GCM is $\omega = 0$. However, we interpolate the data to constant pressure levels, so at the bottom-most level of our analysis the condition $\omega = 0$ does not apply.

Term 7 is the residue term and is a catch-all for sources and sinks not accounted for by the EKE equation. Errors collected by this term include frictional effects, sub-grid processes, errors introduced by the temporal filtering, data assimilation, and interpolation errors. Term 7 is calculated by comparing the right hand side of Eq. (1) to the left hand side by calculating the change of EKE directly using the product rule:

$$\frac{\partial}{\partial t}\langle K_e\rangle = \mathbf{v}' \cdot \frac{\partial \mathbf{v}'}{\partial t} \tag{3}$$

3.1. Quasi-geostrophic omega

The MACDA dataset does not include vertical velocity, $\omega = dp/dt$, so a method of computing ω from temperatures, heights, and horizontal winds is required. Three trials were performed: a kinematic solution, a quasi-geostrophic (QG) solution with homogeneous boundary conditions, and a QG solution with kinematic boundary conditions. To estimate the effectiveness of various methods of calculating ω, trials of each method were run on data from the MGCM simulation of K13 during the same $L_s = 200$–$230°$ period as to be investigated in MACDA and compared to the model provided ω, which is considered the truth.

The kinematic estimation of vertical motion depends on the horizontal divergence and mass continuity:

$$\omega = \int_p^{p_s} \nabla_h \cdot \mathbf{V} dp, \tag{4}$$

where $\nabla_h \cdot \mathbf{V}$ is the horizontal divergence, and p_s is the surface pressure. A second order correction following (O'Brien, 1970) required nonzero values of omega at the top of the atmosphere to be linearly distributed throughout the column.

The initial kinematic solution was found to be inadequate in describing the structure of the vertical motion. It was correlated to the non-pressure-weighted 3D MGCM ω with a coefficient of 0.21 between 10°N and 80°N over the entire $L_s = 200$–$230°$ period. The inability of the method to produce well-behaved vertical motion was expected based on the poor estimation of divergence from horizontal winds via finite differencing. Instead, the traditional form of the QG-ω equation was used to evaluate vertical motion:

$$\left[\nabla_h^2 + \frac{f_0^2}{\sigma}\frac{\partial^2}{\partial p^2}\right]\omega = \frac{f_0}{\sigma}\frac{\partial}{\partial p}[\mathbf{V_g} \cdot \nabla_h(\zeta + f)] + \frac{1}{\sigma}\nabla_h^2\left[\mathbf{V_g} \cdot \nabla_h\left(\frac{RT}{p}\right)\right], \tag{5}$$

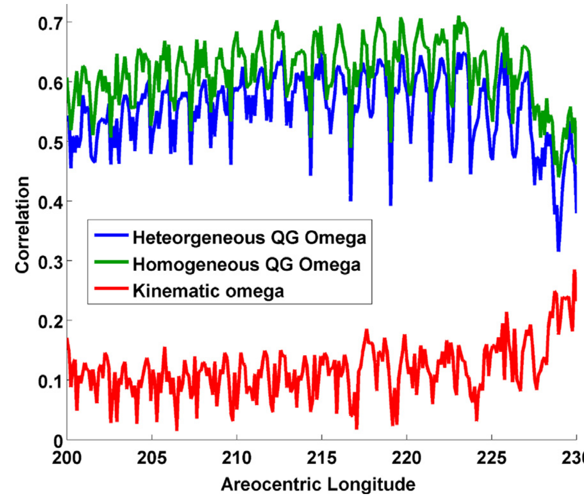

Fig. 4. Correlation of the two forms of quasi-geostrophic ω and kinematic ω to the Kavulich et al. (2013) GFDL simulation ω between 28°N and 80°N for all pressure levels.

where ω is the vertical velocity, $\mathbf{V_g}$ is the geostrophic wind, σ is the static stability, ζ is the relative vorticity, p is the pressure, and f_0 is the Coriolis parameter. Sequential over-relaxation was used to invert the left-hand side Laplacian. Static stability was calculated using the relation $\sigma = \frac{\partial\theta}{\partial p}(RT)/(p\theta)$ and was averaged over each level.

A uniform, homogeneous boundary condition across the entire planet was first attempted and compared to a boundary condition supplied by the kinematic solution. Compared to the control solution of the MGCM, the homogeneous boundary condition solution outperformed the kinematic boundary condition solution. Fig. 4 shows the correlation between the GFDL MGCM ω and QG-ω with homogeneous boundary condition between 28°N and 80°N for $L_s = 200$–$230°$. The oscillating pattern in the correlations in Fig. 4 is the result of the progression of the packets of EKE themselves. The correlation between the QG-omega and model omega is lower when the pressure-averaged EKE is high, and the correlation is high when the average EKE is low. The correlations between the non-pressure-weighted 3D MGCM ω field and the kinematic boundary condition solution and the homogeneous boundary condition solution for the entire $L_s = 200$–$230°$ time series between 10°N and 80°N are 0.55 and 0.62, respectively.

While the correlation of QG-ω to the GFDL MGCM omega is somewhat low during the beginning and end of the study period, the correlations between terms of the EKE equation computed using each of the two vertical motion fields are considerably higher. The GFC, BCEC, BTEC, and residual terms are correlated at 0.96, 0.80, 0.91, and 0.93, respectively. Thus, it is the quasi-geostrophic part of ω that dominates the processes described by the EKE equation. We therefore use the QG-ω with homogeneous boundary conditions as the vertical velocity for the rest of this study.

The time-mean vertical motion during the period $L_s = 200$–$230°$ for two levels is shown in Fig. 5. Shown are MY 24 (left), MY 25 (middle), and MY 26 (right) at the 100-Pa level (top) and 400-Pa level (bottom). Note that the figure is in pressure coordinates so that negative values of motion are upward. A stationary, wavenumber-two structure is clearly visible at the 100-Pa level, with ascending motions to the west of Arabia Terra and the Tharsis Plateau and descending motions on the eastern slopes. A strong wavenumber-two pattern exists as well in the TES retrievals (Banfield et al., 2003). A wavenumber-two structure remains at 400 Pa, but the descending branches are much stronger than the ascending branches, possibly as a result of the Hadley circulation.

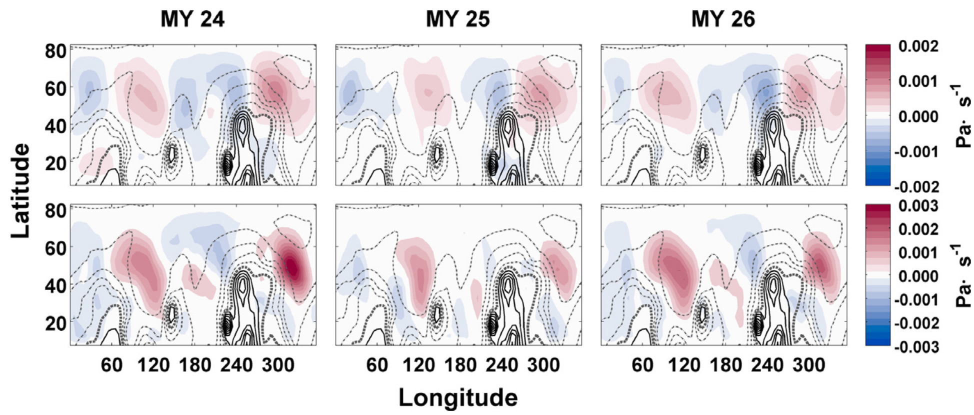

Fig. 5. The time-mean vertical velocities for L_s = 200–230° for the 100-Pa (top) and 400-Pa (bottom) pressure level for MY 24 (left), MY 25 (middle), and MY 26 (right). Contours are surface elevation in 1000 m increments. Values below the mean geoid are dashed with the 0 mean geoid bolded.

3.2. Divergence and geopotential flux

A final obstacle to the implementation of the EKE equation to the MACDA dataset was the lack of data for the horizontal divergence of the wind in the dataset. Initially, the divergence was calculated via finite differencing of the horizontal winds. As with vertical motion, control tests were performed on data from the K13 MGCM simulation. Second, fourth, and sixth-order finite differencing proved inadequate to capture smaller scale patterns in the divergence. The effect was amplified by the lower resolution of the MACDA dataset.

We eliminated the problem by rearranging vector products in the EKE equation. In particular, the geopotential flux convergence term (term two in Eq. (1)) can be rewritten as

$$-\langle \nabla \cdot \mathbf{v}'\phi' \rangle = -\langle \phi' \left(\nabla \cdot \mathbf{v}' \right) + \mathbf{v}' \cdot \nabla \phi' \rangle. \tag{6}$$

This expression involves the horizontal divergence of eddy velocities. Explicitly writing out each term yields

$$-\langle \phi' \left(\nabla \cdot \mathbf{v}' \right) + \mathbf{v}' \cdot \nabla \phi' \rangle = -\left\langle \phi' \frac{\partial u'}{\partial x} + \phi' \frac{\partial v'}{\partial y} + u' \frac{\partial \phi'}{\partial x} + v' \frac{\partial \phi'}{\partial y} \right\rangle. \tag{7}$$

Alternatively, the geopotential flux convergence can be written before the product rule is used to obtain:

$$-\langle \nabla \cdot \mathbf{v}'\phi' \rangle = -\left\langle \frac{\partial (u'\phi')}{\partial x} + \frac{\partial (v'\phi')}{\partial y} \right\rangle. \tag{8}$$

In this way, the horizontal divergence is no longer required in the calculations. Only products of heights and winds are necessary to evaluate the GFC term. The method of calculating GFC using Eq. (8) is superior as it requires only one finite difference calculation as opposed to the two finite differences required by equation Eq. (7). The use of divergence in evaluating the transport term is avoided in a similar way.

4. Results

4.1. Pressure-weighted vertical averages

The pressure-weighted terms of the eddy kinetic energy equation are shown in Fig. 6. Shown are the eddy kinetic energy (top), baroclinic energy conversion (second row), geopotential flux convergence (third row), eddy kinetic energy transport (fourth row), barotropic energy conversion (fifth row), and residue (bottom). The left, middle, and right columns are MY 24, 25, and 26, respectively. The strongest EKE and its sources and sinks are found away from the equator. The EKE in each MY is at a maximum in a band between 50°N and 80°N, with the highest values between 100°E and 200°E and a secondary maximum in MY 24 and 26 near 330°E. This pattern can be explained by stationary waves caused by high topography directly upstream of the favored EKE areas that modulate the propagation of the wave packets (Chang and Orlanski, 1993). The EKE maximum in MY 25 is approximately half the value of the two non-GDS years. The EKE average can most closely be compared to Fig. 4 (top) of Mooring and Wilson (2015) that shows an inter-annual mean of EKE for all three MACDA years at one level during their PRE season (L_s = 155–235°) and their Fig. 10, which shows the MY 24/26 average compared to MY 25 during the dust period (L_s = 186–275°). The Mooring and Wilson (2015) figures show that EKE is favored in certain meridional areas, namely the Planitias, and that eddy activity is reduced in MY 25 during the GDS.

We find the cause for the decreased maximum in EKE in MY 25 to be the reduction of BCEC, which shows a structure similar to the EKE. Positive baroclinic energy conversion is contained in the 50–80°N band and in MY 24 and 25 has a maximum collocated with the eddy kinetic energy maximum. The reduced BCEC in MY 25 is due to the GDS throughout the time studied. MY 26 has a bifurcated BCEC maximum on either side of the EKE maximum. The westerly maximum is displaced to 70°E, and the location upstream is explained by orographic effects due to stronger subsidence on the leeward side of Arabia Terra (see Fig. 5). These zonal differences in the placement of BCEC between MY 24 and 26 to are most likely due inter-annual variability.

As stated earlier, the geopotential flux convergence and eddy kinetic energy advection are transport terms. Thus, they cannot be the ultimate source or sink of EKE, but they can contribute to local changes in the EKE. The GFC is the strongest local source and sink of all generation terms and shows a structure dependent on topography. Minima of geopotential flux occur, in general, in the Planitias and downwind of high topography. Maxima of GFC exist over the Plateaus and upstream of topography. The primary minimum occurs around 180°E in the band of highest EKE and carries energy downstream to the north of the Tharsis Plateau, where it is deposited to help extend the storm track to the east away from the strongest BCEC, in agreement with Banfield et al. (2004) and Hinson and Wang (2010). [This phenomenon also exists terrestrially over the Pacific Ocean (Chang, 1993; Chang and Orlanski, 1994).] The mechanism of extending the EKE band eastward occurs in all three years but is strongest in MY 24.

The eddy kinetic energy advection plays an important role in MY 26 in transporting the energy generated by the westerly shifted BCEC maximum to the channel of maximum EKE in Utopia Planitia.

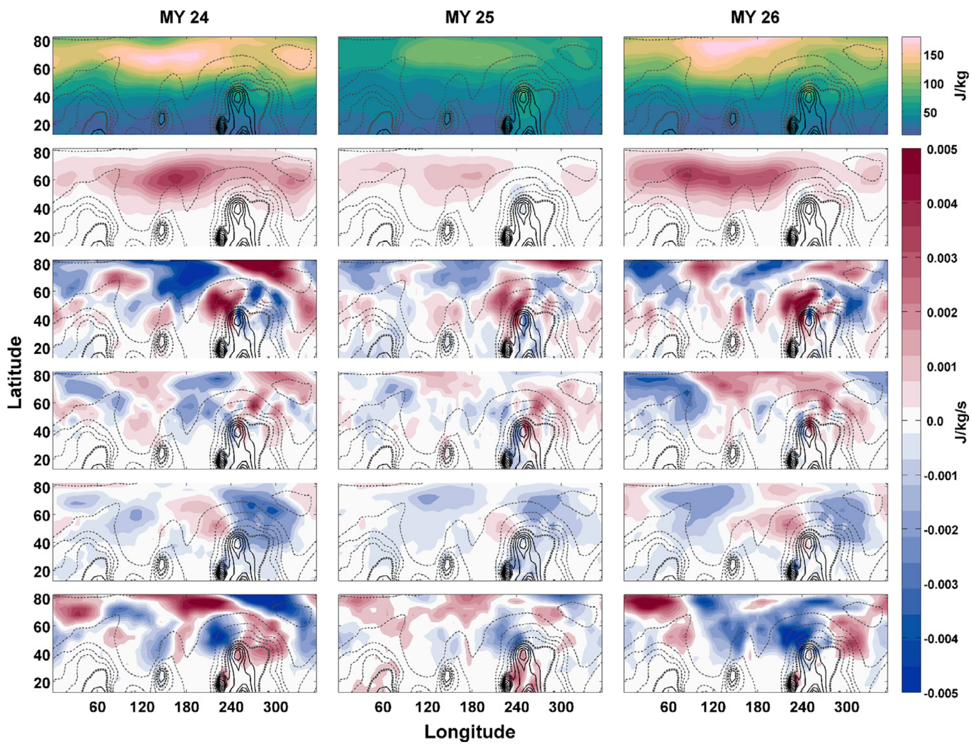

Fig. 6. Pressure-weighted vertical averages of the time mean of the terms of the eddy kinetic energy equation for L_s = 200–230° for MY 24 (left column), MY 25 (center column), and MY 26 (right column). Shown is the eddy kinetic energy (top), baroclinic energy conversion (second row), geopotential flux convergence (third row), the eddy kinetic energy transport (fourth row), the barotropic energy conversion (fifth row), and the residue (bottom). Contours are surface elevation in 1000 m increments. Values below the mean geoid are dashed with the 0 mean geoid bolded.

A sink of energy occurs north of Arabia Terra with a source to the east in Utopia Planitia, depositing the EKE generated by the BCEC maximum at the lower elevation. A similar arrangement of sources and sinks is also present in MY 24 and MY 25, but in those years the western BCEC maximum is much weaker. In MY 24, the maximum of transport is collocated with the EKE maximum near 330°E, which along with the stronger maximum in GFC could explain why the eastern EKE maximum is stronger in MY 24 than in MY 26.

The barotropic energy conversion acts mostly as a sink of EKE. There are two main areas of negative BTEC: a primary minimum over the Tharsis Plateau and a secondary area between 100°E and 120°E near 60°N. MY 25 has a weaker sink of BTEC. As will be explained in more detail later, both of these areas are near the locations of the strongest westerly jet. This suggests that the conversion of eddy potential energy into eddy kinetic energy by BCEC strengthens the jet via BTEC. Finally, the residue is large in magnitude near the pole. The large negative values of the residue must be due to frictional effects, but the positive values at some locations suggest that other factors must also contribute. One such potential source is computational errors in the GFC, as the GFC and residue terms are highly (negatively) correlated with coefficients of −0.89, −0.86, and −0.84 for each year, respectively (a similar observation was reported terrestrially by Ahmadi-Givi et al., 2014). Also, large errors could be caused by the data assimilation scheme that forces the MGCM to alter the atmospheric temperature profile, which in turn modifies the EKE. Although the residual is the same order of magnitude as the other terms in the EKE equation, the overall EKE budget should remain intact as the errors primarily contributing to the residue seem to be due to features unrelated to the eddy kinetic energy equation itself (Ahmadi-Givi et al., 2014).

In comparing Fig. 11 of K13, which used a zonally averaged dust scenario from MY 24, to the left column of Fig. 6, several differences emerge. The BCEC maximum is shifted to the east in MACDA MY 24 compared to the K13 simulation, and the GFC term has a stronger relative magnitude compared to the other terms. To explain these differences, we first note that the dust scenario in K13 is forced zonally to the MY24/25 scenario, so longitudinal details like particular regional dust storms are lost. Individual regional dust storms can be connected to the transient eddies we investigate, and by smoothing these out zonally, the free-running model of K13 could be missing specific events during the L_s = 200–230° period that contribute to the pressure-weighted averages. Free-running simulations can deviate substantially from observations, so that if the simulation used by K13 incorrectly modeled the strength, number, or location of transient events, the averages could have been shifted. Further corroborating this possibility is a comparison of the Hovmöller of K13 (their Fig. 10) to the MACDA MY 24 (Fig. 3). While the frequency of waves is similar, the coherence and relative strength differ. Waves in the K13 simulation are strikingly more coherent than those prescribed by MACDA. Indeed, MY 26 BCEC and GFC are closer to that of K13 than the MY 24 scenario, suggesting that the simulation of K13, while forced by a particular dust scenario, is only one possible scenario for the evolution of the martian atmosphere.

4.2. Zonal and meridional averages

4.2.1. Eddy kinetic energy

Zonal (left column) and meridional (right column) means for the eddy kinetic energy for the L_s = 200–230° period are contoured in Fig. 7. The EKE is at a maximum near 10 Pa in the 50–80°N latitude band. The location of the highest EKE in the region of the westerly jet agrees with K13 and other studies, including Barnes et al. (1993). This corroborates the assertion that the EKE contributes to the maintenance of the westerly jet through BCEC and BTEC. [However, we note that the jet is strongest in MY 25 (see Fig. 2) when EKE is weakest. This is due to the jet becoming more thermally driven as a result of the stronger meridional

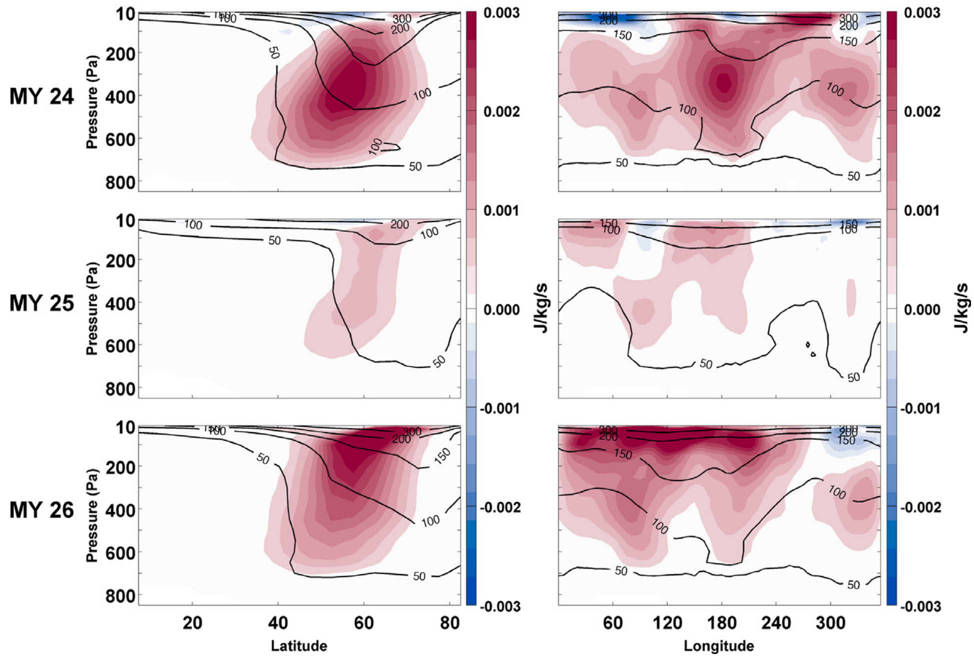

Fig. 7. Vertical cross sections of the time-mean (L_s = 200–230°) of the zonal mean (left column) and meridional mean (right column) of baroclinic energy conversion, $-\omega'\alpha'$ and the eddy kinetic energy (J/kg) contoured. The meridional mean is computed for the 57.5–82.5°N latitude band. Results are shown for MY 24 (top), MY 25 (middle), and MY 26 (bottom).

temperature gradient in the mid-levels, which is a positive feedback mechanism between increased dust loading and a strengthened Hadley cell (Basu et al., 2006; Haberle et al., 1993).] The effect of dust on MY 25 is evident as the maximum is below 325 J/kg. In the meridional average, there are two main areas of EKE. In MY 24, the maximum occurs near 300°E with a secondary maximum near 100°, while in MY 26 a more elongated maximum is located near 100°E. MY 25 has a decreased, bifurcated maximum at 150°E and 250°E. The dissimilar meridional distributions of EKE in the non-GDS Mars years are a result of the different energy conversion processes discussed below.

4.2.2. Geopotential flux convergence

The total geopotential flux convergence, $-\overline{\nabla_3 \cdot \mathbf{v}_3'\phi'}$, is shown in Fig. 8 with the zonal average on the left and meridional average on the right for L_s = 200–230°. In the zonal average, three main areas of geopotential flux convergence and divergence are prominent. Geopotential flux divergence occurs north of 40°N and below 40 Pa, is strongest in MY 26, and is weakest and lower in height in MY 24. A second divergent area exists generally south of 40°N, above 40 Pa, and is strongest and slightly further north in MY 24 and weakest and further south in MY 26. Between these divergent areas, convergence of geopotential fluxes occurs at 20 Pa near 60°N and is weakest in MY 25. As the geopotential flux term is neither a global source nor a global sink of EKE, it is expected that the reduction in magnitude during MY 25 should be not as great as for the terms that can be affected by changes in opacity, since the geopotential flux term would transport EKE that already exists prior to the onset of increased optical depth.

Geopotential flux is weak at the surface and stronger above 10 Pa (not shown). Meridionally, convergence is favored between 100°E and 150°E in all years while the strongest divergence occurs just to the west between 0°E and 100°E. These features can be understood by considering the atmospheric column shrinking due to strong ascent over Arabia Terra followed by the atmospheric column stretching to the east of that plateau. As the atmospheric column shrinks on ascending over Arabia Terra, divergence must take place to preserve mass, and the converse is true as parcels descend on the leeward side of the plateau. The convergence on the downstream side of the high topography is reflective of the lee cyclogenesis found by Greybush et al. (2013). In MY 24, this pattern repeats with the Tharsis Plateau. There is strong convergence west of 240°E with strong divergence just to the east.

4.2.3. Baroclinic energy conversion

Baroclinic energy conversion plays a key role in sustaining synoptic-scale systems in the martian atmosphere and is characterized by the upward and poleward transport of heat. The zonal (left) and meridional (right) averages of $-\langle\omega'\alpha'\rangle$ are shown in Fig. 7. Zonally, there exists a single maximum in each Mars year centered along 60°N. The vertical placement differs between years: in MY 24, the maximum is located near 500 Pa, but is above 100 Pa in MY 26. The MY 25 maximum is so weak as to not have a well defined absolute maximum. A minimum in BCEC exists in the upper levels near 40 Pa in MY 24 and 25, but the feature is weaker in MY 26. This low-dust-loading behavior was also echoed in the baroclinic conversion found by Greybush et al. (2013). As in K13, this minimum can be partially explained by GFC in those regions; convergence of heights in those areas forces subsidence. The BCEC term becomes negligible at all latitudes and longitudes above 10 Pa. (not shown).

In the meridional direction, the preferred regions of BCEC occur mainly between 0°E and 200°E (throughout Utopia Planitia and Amazonis Planitia), with a second area near 320°E (along the southern edge of Acidalia Planitia) below 100 Pa. The height of the maximum areas of BCEC again differs between years. In MY 24, the conversion area is much shallower and is located below 200 Pa. In MY 25 and 26, maxima occur along and above 10 Pa, with a maximum in MY 26 at 100°E and 30 Pa, which is located where the strongest minimum occurs in MY 24. The upper level minimum in BCEC in MY 24 can be explained again by considering the GFC term. The results for MY 25 and 26 agree with those of K13 on a secondary maximum of BCEC above 100 Pa near 100°E.

The BCEC term is substantially reduced in MY 25 compared to MY 24 and 26, with the MY 25 maximum at 60°N reduced by an order of magnitude compared to the clear years. Additionally, the

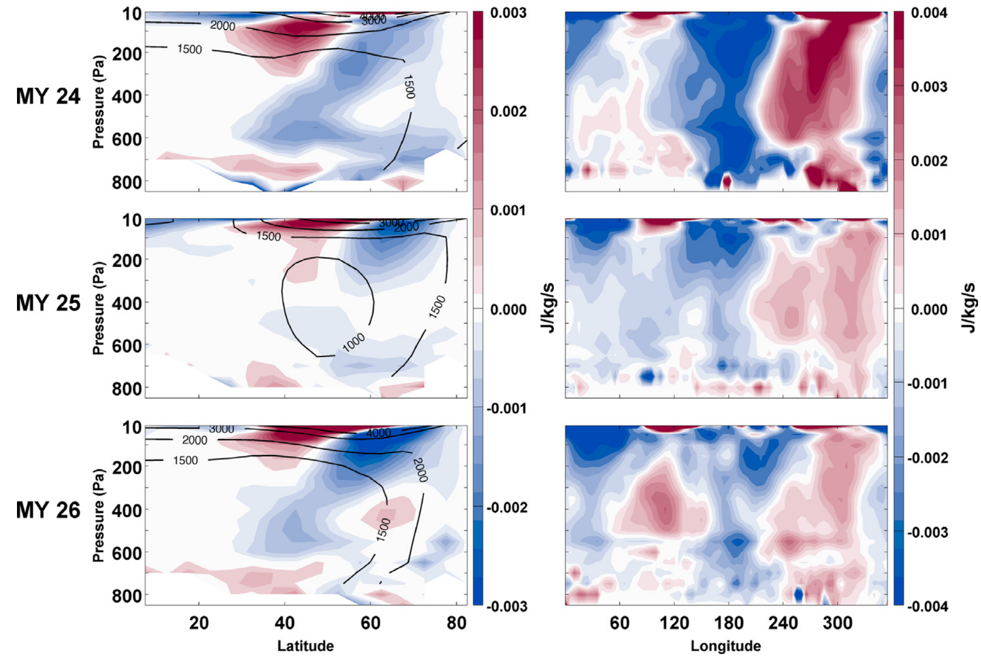

Fig. 8. Vertical cross sections of the time-mean (L_s = 200–230°) of the zonal mean (left column) and meridional mean (right column) of geopotential flux convergence, $-\overline{\nabla_3 \cdot \mathbf{v}_3' \phi'}$. The meridional mean is computed for the 57.5–82.5°N latitude band. Results are shown for MY 24 (top), MY 25 (middle), and MY 26 (bottom). Contours show the standard deviation of the geopotential height (gpm).

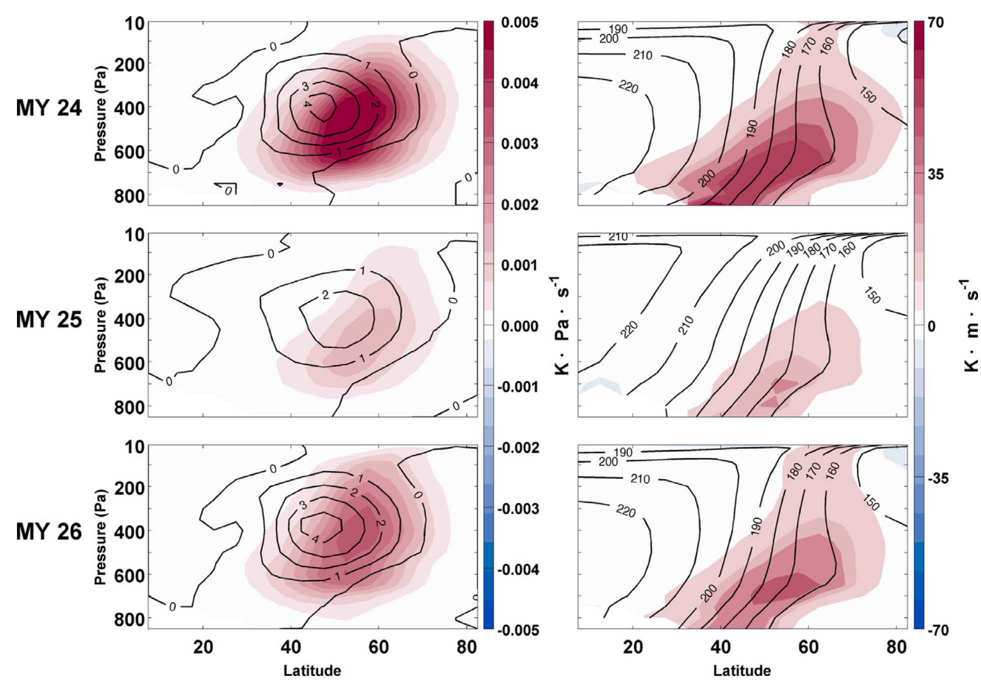

Fig. 9. Vertical cross sections of the time-mean (L_s = 200–230°) of the zonal mean of the vertical heat flux, $-\overline{T'\omega'}$, (left column) and meridional heat flux, $\overline{T'v'}$, (right column). Results are shown for MY 24 (top), MY 25 (middle), and MY 26 (bottom). Contours show temporal mean of vertical motion (100 μ Pa/s) (left) and temporal mean of temperature field (K) (right).

positive energy conversion in the meridional average west of 200°E in MY 24 and 26 is absent in MY 25.

4.2.4. Heat flux

Baroclinic instability is characterized by poleward and vertical transport of heat. The reduction in heat flux in MY 25 (middle row) compared to MY 24 (top) and MY 26 (bottom) is shown in Fig. 9. The vertical heat flux, $-\overline{T'\omega'}$, is at left, and the meridional flux, $\overline{T'v'}$, is at right. Each year contains areas of coincident vertical and poleward heat flux between 40°N and 70°N. MY 24 contains the strongest vertical fluxes, followed by MY 26; MY 25 has substantially weakened vertical fluxes, suggesting that some mechanism is suppressing the conversion of eddy available potential energy into eddy kinetic energy. The vertical flux is confined to between the surface and 100 Pa, and no downward flux is observed. The meridional flux displays the same reduction in strength from MY 24 to 26 to 25 with the strongest flux confined between 800 and 100 Pa. MY 26 has slightly stronger vertical and meridional fluxes above 200 Pa, which explains the height of the BCEC maximum in MY 26. The pattern of reducing heat flux in the surface to 100 Pa

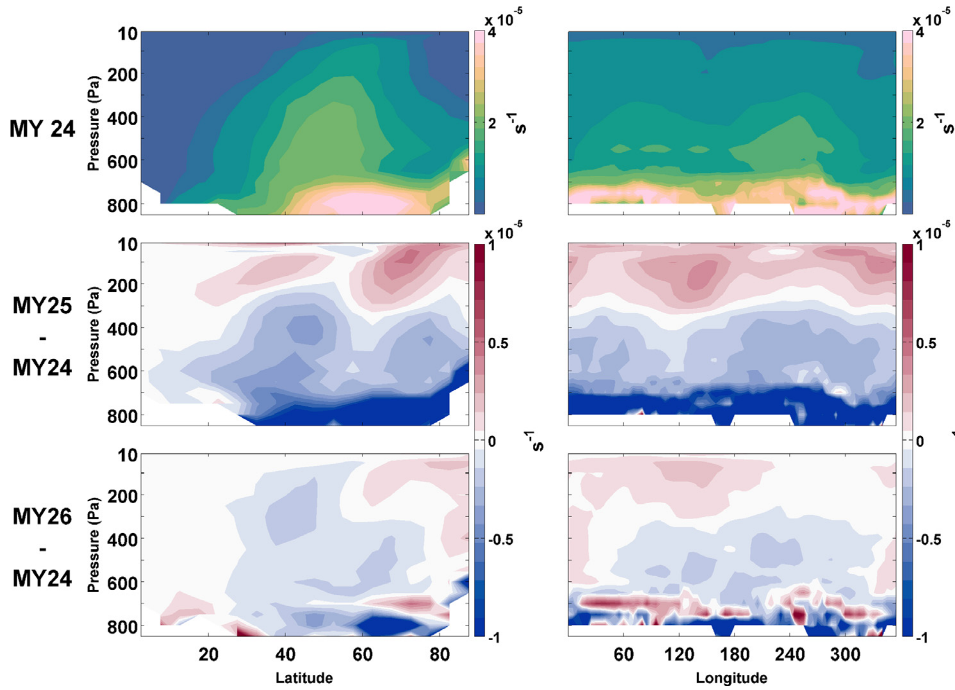

Fig. 10. Vertical cross sections of the time-mean (L_s = 200–230°) of the zonal mean (left column) and meridional mean (right column) of the Eady index. The meridional mean is computed for the 57.5–82.5°N latitude band. Results are shown for MY 24 (top), the difference between MY 25 and MY 24 (middle), and the difference between MY 25 and MY 24 (bottom).

region from MY 24 to 26 to 25 can be attributed to the increasing dustiness from one year to the next, altering the vertical temperature profile.

4.2.5. Eady index

To help explain the underlying cause of the reduced heat fluxes, and thus the reduced baroclinic energy conversion, the structure of the baroclinic instability itself must be explored. There are three reasons that BCEC could be reduced: (i) the static stability of the atmosphere is increased, (ii) the vertical wind shear is weakened, or (iii) some other mechanism prevents the development of perturbations that could efficiently convert available potential energy into eddy kinetic energy.

The Eady index, σ, (Hoskins and Valdes, 1990) is often used to quantify the sensitivity of the flow to baroclinic instability. It is defined as the ratio between the vertical shear in the zonal wind and the Brunt–Väisälä frequency (N), a measure of static stability, such that

$$\sigma = 0.31 f\left(\frac{\partial u}{\partial z}\right)(N)^{-1}, \tag{9}$$

where u is the zonal wind component, and f is the Coriolis parameter. N is defined as

$$N = \left(\frac{g}{\theta_{va}}\frac{\partial \theta_{va}}{\partial z}\right)^{\frac{1}{2}} \tag{10}$$

where g is the gravitational constant, and θ_{va} is the ambient virtual potential temperature. A higher Eady index indicates a stronger sensitivity of the flow to baroclinic instability.

The left column of Fig. 10 shows a vertical cross section of the zonal average of the Eady index, and the right column is a meridional average for a latitudinal band of 57.5–82.5°N. Shown are MY 24 (top), the difference between MY 25 and MY 24 (middle), and the difference between MY 26 and MY 24 (bottom). The meridional cross section is restricted to the 57.5–82.5°N band as that is where a vertical average of the Eady index (not shown) and BCEC (Fig. 6, second row) are at a maximum. In the zonal direction, all three years show large-scale similarity with the absolute maximum in a narrow band at the surface extending from 40°N to 80°N. Large index values protrude vertically from the surface at 50°N polewards to 60°N at ~70 Pa. MY 26 is slightly weaker below 300 Pa and slightly stronger above 300 Pa near the pole but does not deviate substantially from the MY 24 average. MY 25 has larger Eady index above 300 Pa between 60°N and 80°N but much weaker surface to 300 Pa values. This lower area is responsible for the reduced heat fluxes in Fig. 9.

To further investigate the inhibition of energy conversion, the time-mean vertical Brunt–Väisälä frequency profile (top), vertical wind shear (middle), and potential temperature gradient (bottom) for L_s = 200–230° for each MY are shown in Fig. 11. Above 300 Pa, both the static stability and the vertical wind shear are increased in MY 25 compared to MY 24 and 26. [Note that the increased vertical wind shear above 300 Pa in MY 25 is the result of the strengthened westerlies, which keep an approximate thermal wind balance with the increased meridional temperature gradient (Fig. 2).] Below 300 Pa, which is the area of greatest eddy heat flux (Fig. 9), both the static stability and vertical wind shear act together in lowering the Eady index in MY 25. Between 500 and 300 Pa, the Brunt–Väisälä frequency is larger in MY 25, with MY 26 in between MY 24 and 25. The higher stability is due to the altered vertical temperature profile. Potential temperatures are lower in the 500–200 Pa layer in MY 25, and consequently, the potential temperature gradient is larger from 500 Pa up in MY 25 (Fig. 11, bottom panel). MY 26 having a stability profile between that of MY 24 and MY 25 is the result of the regional dust storm at L_s = 215°, which contributes to the warmer temperature profile in MY 26 compared to MY 24. Between 500 and 800 Pa, the vertical wind shear is reduced in MY 25 from MY 24, with MY 26 between. The reduction in shear is the result of increased surface winds in dust storm years (Haberle et al., 1993), which reduces the difference between winds at the top of the boundary layer and below the westerly jet, limiting the shear. Above 200 Pa,

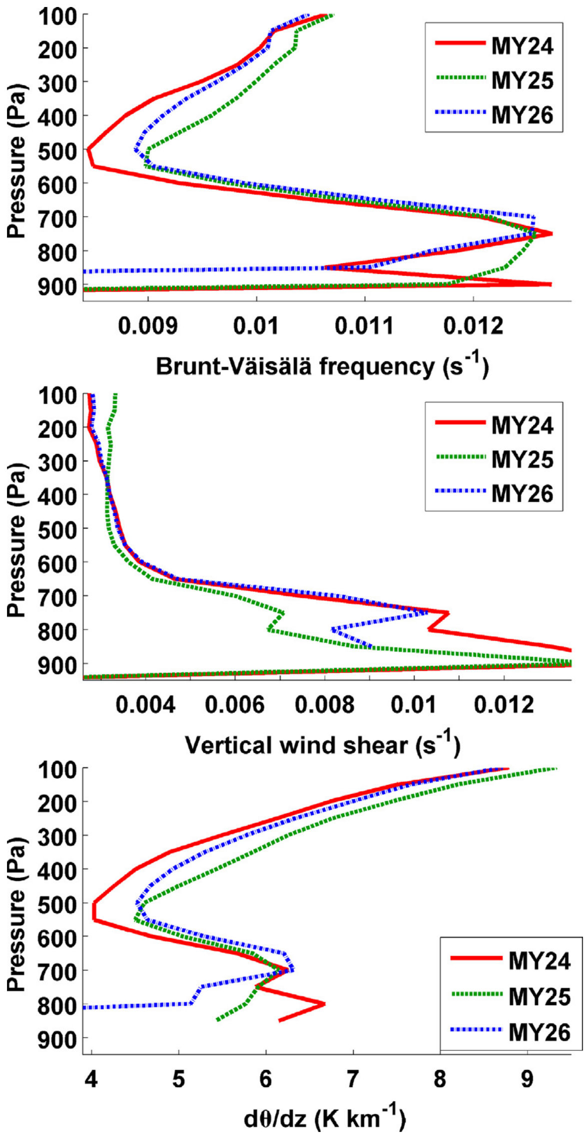

Fig. 11. Brunt–Väisälä frequency vertical profile (top), vertical wind shear (middle), and potential temperature gradient (bottom) for the time-mean L_s = 200–230° of the 57.5–82.5°N latitude band.

the Brunt–Väisälä frequency is smaller in MY 26, which explains the increased heat fluxes aloft compared to MY 24.

4.2.6. Barotropic energy conversion

Barotropic energy conversion is found to be a major sink of EKE, especially near 10 Pa. Fig. 12 displays the zonal (left panels) and meridional (57.5–82.5°N band) (right panels) averages of the time-mean of barotropic energy conversion for the L_s = 200–230° period. Zonally, there are two separate minima: one between 30°N and 60°N above 50 Pa and another near 70°N between 10 Pa and 100 Pa. The secondary minimum is collocated with the axis of highest EKE (Fig. 7, contours). This suggests that the baroclinic eddies transfer kinetic energy to the basic flow, strengthening the jet, similar to that found by K13 and terrestrially (Orlanski and Katzfey, 1991) with the rate of growth baroclinically similar to the rate of decay barotropically as found by Simmons and Hoskins (1978). The meridional areas of negative BTEC coincide with the strongest zonal winds (contoured). Each Mars year has two areas where BTEC transfers kinetic energy from the eddies to the flow that strengthens the westerly jet. These areas are located near 90°E and 290°E, with the western MY 25 maximum shifted to 150°E. An exception is the eastern maximum in MY 26 that has positive BTEC located on the upstream side of the zonal wind maximum, but the zonal wind maximum associated with that area is the weakest of the maxima. Here, kinetic energy is being transferred from the jet to the eddies, weakening that jet maximum in MY 26.

The non-barotropic nature of the non-GDS years follows that found by Barnes et al. (1993) and is in contrast to Banfield et al. (2004), who found that the waves weakened rather than strengthened the jet while shifting its center either north or south. We attribute the discrepancy between the results presented here and Banfield et al. (2004) to differences between direct observations and reanalyses. The TES observations used by Banfield et al. (2004) are insensitive to the bottom scale height – the usual source of BCEC. Those observations favor the detection of activity higher in the atmosphere where BTEC is more prevalent. Though MY 24 and MY 26 are more in character with the baroclinic situation of Barnes et al. (1993), a slightly more barotropic situation exists for MY 25. While the BTEC is still negative, the magnitude is reduced. As will be shown in discussing the development of an individual eddy in MY 25, the weaker magnitude of the BTEC average in MY 25 is not simply a matter of less EKE transferred to the mean flow (Fig. 7, contours) but that the BTEC plays a more prominent role in the generation of EKE at some times and locations than in the other two years.

4.2.7. Transport

Finally, the EKE advection term does contribute to the transport of EKE across the hemisphere, as is shown in Fig. 13. In the meridional average, the transport term redistributes the EKE similarly to the GFC term. That is, energy is transported from the main BCEC areas, namely near 60°E and 200°E (Fig. 7) downstream to 150°E and 300°E, mostly near 10 Pa. EKE transport by the flow and GFC elongate the region of highest EKE to the east, so much so that in MY 24, a strong band of EKE (>120 J/kg) exists around the entire 70°N latitude circle (see top left panel of Fig. 6). The eastward stretching of the high EKE region is well known from terrestrial studies (e.g. Chang, 1993). Zonally, the EKE transport and GFC terms are also reinforcing. The role of the transport processes becomes even more transparent when the two transport terms are combined (Fig. 13, contours). In the zonal average, the combined transport terms can be seen to be at a maximum near 10 Pa in the regions south of the highest EKE, between 40°N and 50°N. Energy is taken out of the main generation area and deposited to the south, extending the area of EKE southward. Closer to the surface the negative region extends equator-ward with a region of weakly positive EKE transport near the pole, but the combined transport (Fig. 13, contours) shows no such near surface secondary maximum as the GFC is weak near the pole in the zonal average.

5. Contrasting prototypical waves in clear and dust storm years

5.1. MY 24 example storm

To further elucidate the differences between EKE generation processes in dust and clear periods, a typical wave from each MY 24 and MY 25 is contrasted. They are indicated on Fig. 3 by lines A and B, respectively. We begin with a MY 24 energy center, which is generated from downstream development beginning at L_s = 206.6°, and follow its progression until L_s = 209.1° (Fig. 14, left column). Each panel advances time by 0.5 Sol compared to the panel above. The EKE packet is initiated to the northeast of Arabia Terra and propagates eastward at a rate of approximately 90° Sol^{-1} until it dissipates after completing nearly one circumnavigation. This is typical of storms in the clear years with the area of development and dissipation and its generation terms duplicated multiple times over the study period. These preferred areas of

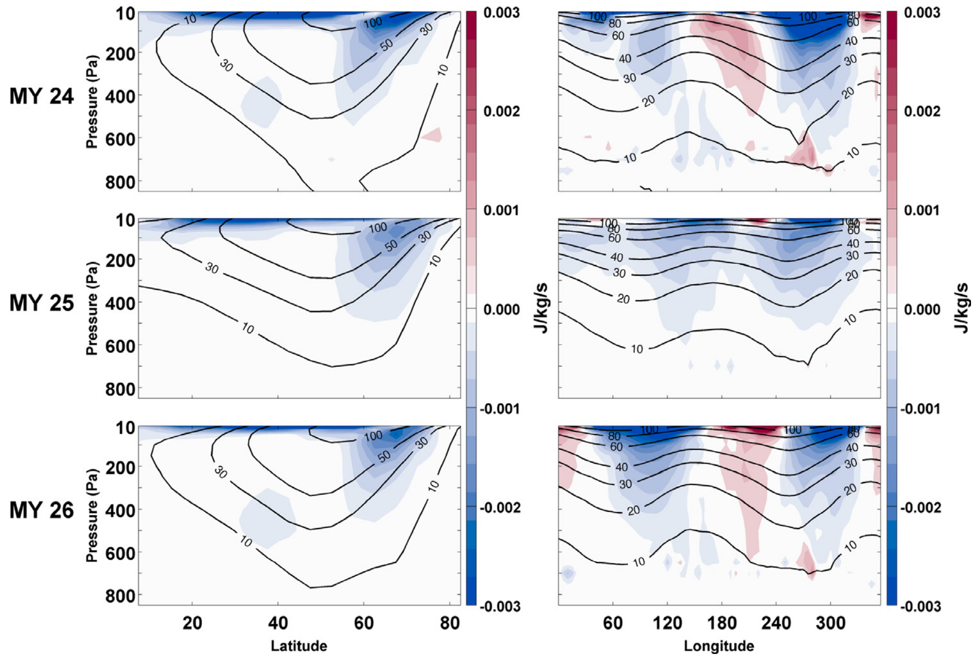

Fig. 12. Vertical cross sections of the time-mean ($L_s = 200–230°$) of the zonal mean (left column) and meridional mean (right column) of barotropic energy conversion, $-\mathbf{v}' \cdot (\mathbf{v}_3' \cdot \nabla_3)\mathbf{v_m} - \mathbf{v}' \cdot \overline{(\mathbf{v}_3' \cdot \nabla_3)\mathbf{v}'}$. The meridional mean is computed for the 57.5–82.5°N latitude band. Results are shown for MY 24 (top), MY 25 (middle), and MY 26 (bottom). Contours show zonal average zonal wind (m/s) (left) and meridional average zonal wind (m/s) (right).

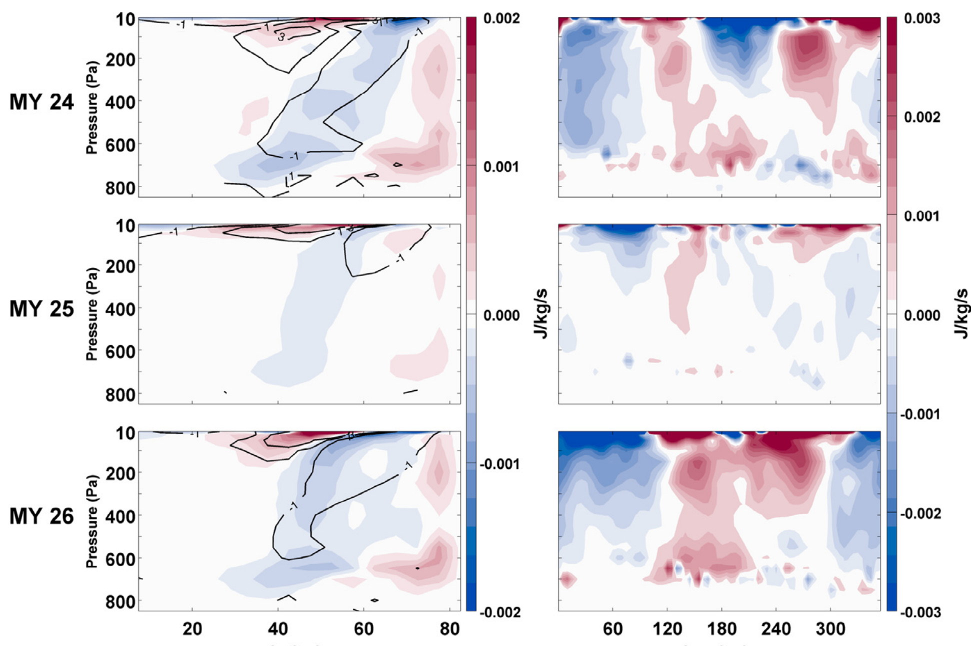

Fig. 13. Vertical cross sections of the time-mean ($L_s = 200–230°$) of the zonal mean (left column) and meridional mean (right column) of EKE transport, $-\nabla \cdot \mathbf{v}K_e$. The meridional mean is computed for the 57.5–82.5°N latitude band. Results are shown for MY 24 (top), MY 25 (middle), and MY 26 (bottom). Contours show average total EKE transport, $-\nabla \cdot \mathbf{v}K_e - \overline{\nabla_3 \cdot \mathbf{v}_3'\phi'}$ (mJ/kg/s).

development are locations of lee cyclogenesis (Greybush et al., 2013) and are the storm tracks noted by Hollingsworth and Barnes (1996), Banfield et al. (2004), Wang et al. (2005), Basu et al. (2006), and Hinson and Wang (2010).

The two transport terms are also shown in Fig. 14. The GFC is the middle column, and the EKE transport term is at right. The GFC term is the largest local contributor to the transport of EKE. As in the terrestrial atmosphere, the geopotential flux is the initiator of EKE generation. In the initial phase of development, the generation of EKE is preceded by GFC (top row). At the next step (row two), the GFC maximum has an EKE maximum slightly downstream, and they travel together as time progresses, following the development paradigm of (Orlanski and Sheldon, 1995). As the positive region of GFC grows, the EKE grows slightly downstream. However, as the region of positive GFC grows in size and magnitude, an upstream region of geopotential flux divergence intensifies concurrent with the initial region of geopotential flux convergence decaying. The couplet changes in magnitude and size proportionally so that their net contribution is approximately zero. An additional, weaker couplet of GFC forms downstream of

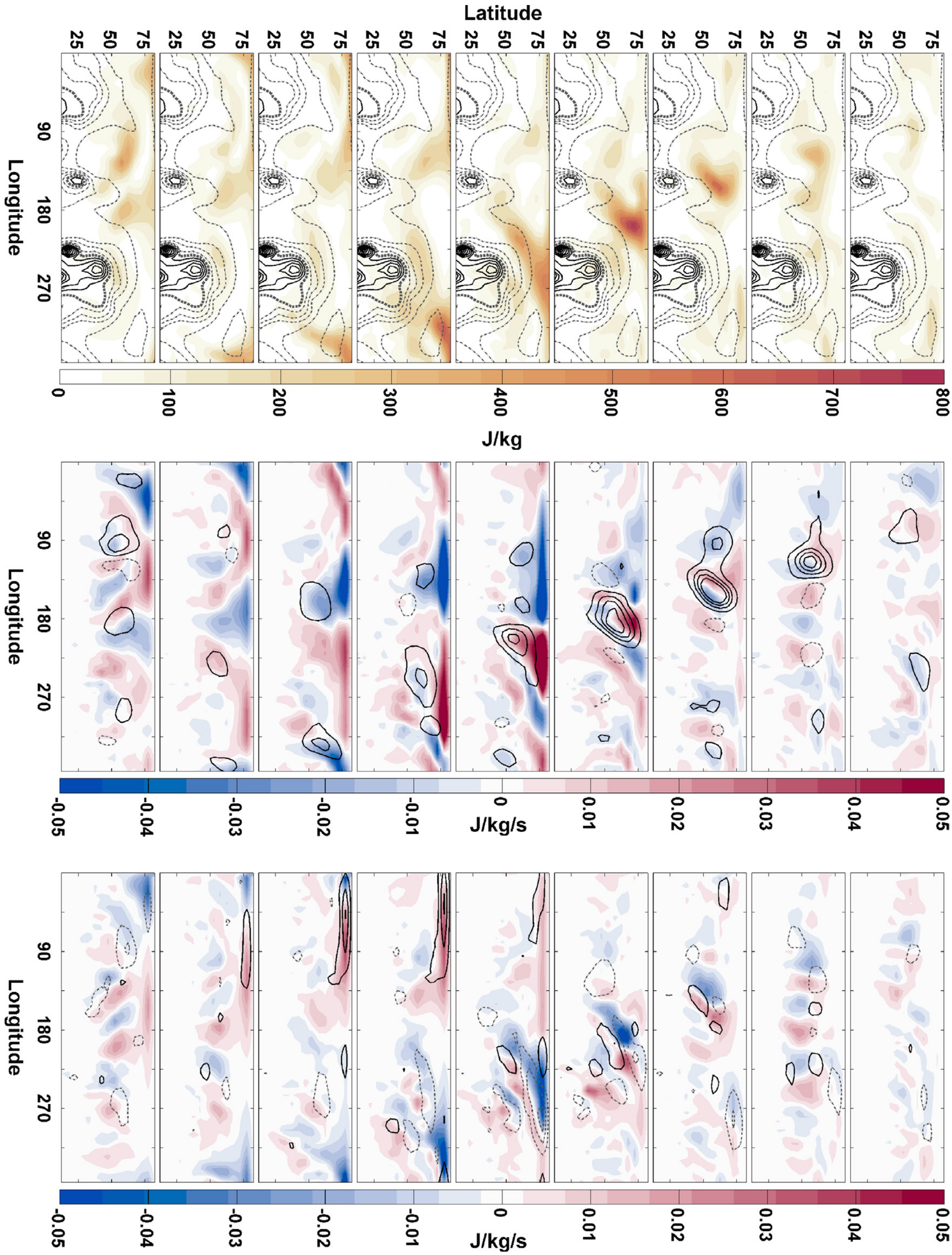

Fig. 14. Time series of vertical, pressure-weighted averages of eddy kinetic energy (left) with topography contoured as in Fig. 6, geopotential flux convergence (middle) with baroclinic energy conversion contoured at 0.008 J/kg/s increments and negative values dashed, and eddy kinetic energy transport (right) with barotropic energy conversion contoured at 0.008 J/kg/s increments and negative values dashed for a 4-Sol period traveling wave in MY 24 beginning at $L_s = 206.6^\circ$ and continuing at 0.5 Sol steps until $L_s = 209.1^\circ$.

the main couplet that helps to disperse energy downstream to trigger further downstream development (Orlanski and Katzfey, 1991). This is consistent with the numerical study of Orlanski and Chang (1993), who found multiple regions of GFC developed after the initial disturbance. The EKE transport term is weaker and has the opposite sign in areas of strongest GFC with a correlation of −0.62 between the pressure-averaged EKE transport and GFC at the middle time step. The transport term propagates the energy eastward from the upstream to the downstream side of the wave as the GFC accumulates energy on the upstream side of the wave.

The generation terms are contoured in Fig. 14. The BCEC (middle column contoured in 0.008 J/kg/s increments) is a source of EKE during the growth phase of the wave packet. The BTEC (right column contoured in 0.008 J/kg/s increments) acts as a sink during

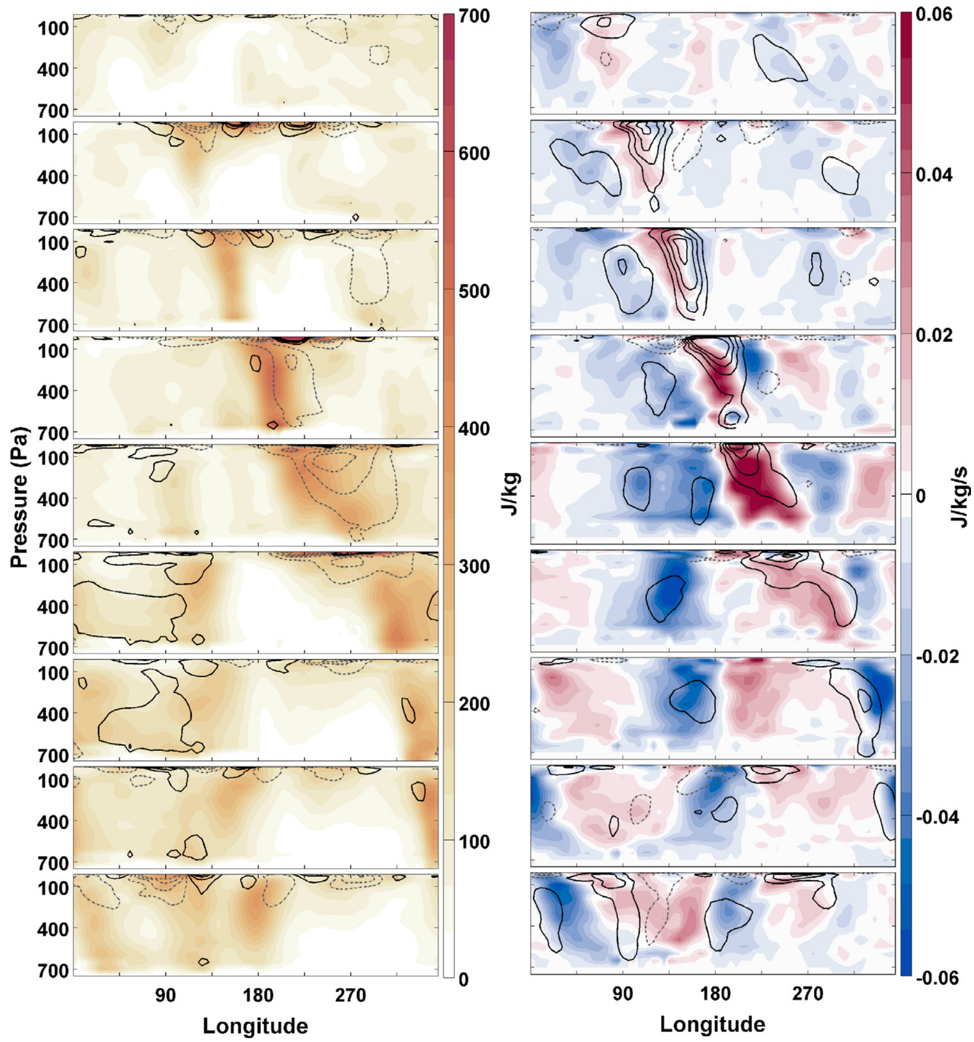

Fig. 15. Time series of the meridional average of eddy kinetic energy (left) with barotropic energy conversion contoured in 0.006 J/kg/s increments and negative values dashed and geopotential flux convergence (right) with baroclinic energy conversion contoured in 0.006 J/kg/s increments and negative values dashed in the 57.5–82.5°N latitude band for the wave in Fig. 14.

the decay phase of the storm. Both of these processes are smaller in magnitude than either of the transport terms. The growth of the EKE maximum occurs due to the input of energy through baroclinic conversion, though the geopotential flux initiates that baroclinic conversion. The top row shows only a weak area of BCEC at the initial time step. Once BCEC begins, the center of BCEC grows quickly as it crosses Utopia Planitia, intensifying the EKE maximum. The baroclinic growth explains the strengthening couplet of GFC, which increases in magnitude as the transport of EKE increases. Thus, GFC initiates BCEC, but the baroclinic growth of the EKE is why the geopotential flux increases in magnitude. The BCEC intensifies until the BTEC begins increasing to the north of the Tharisis Plateau (row three). In row five, the BTEC reaches a minimum, and the EKE packet begins to dissipate.

The baroclinic growth of the EKE is dependent on the ability of waves of the type depicted in this section to simultaneously transport heat towards the pole (converting available potential energy of the mean flow to eddy available potential energy) and vertically (converting the eddy available potential energy to EKE). Next, the continually increasing EKE must be transported downstream. This is not accomplished by the mean flow (Orlanski and Katzfey, 1991) but via propagation by the GFC. Convergence of geopotential heights behind the eddy convert EKE into potential energy, and divergence of geopotential heights ahead of the eddy converts that potential energy back into EKE. [Note that in the text we have referred to positive values of the GFC term as convergence and negative values as divergence due to the minus sign in front of the GFC term.] The wave propagates to the east towards the Tharsis Plateau. The direction of horizontal and vertical heat fluxes reverse as flow expands into Acidalia Planitia, but from Fig. 7 we see the longitudinal average of BCEC is still positive on the at 300 E. Instead of transporting warm perturbations north and up, the topography is helping transport cold perturbations south and down.

The vertical structure of the wave is shown in Fig. 15. The strongest EKE (Fig. 15, left column), GFC (Fig. 15, right column), and BCEC (Fig. 15, contoured right column) are collocated during the strengthening phase of the eddy. The GFC and the BCEC both show westward tilts with height, as expected of a wave converting potential energy into EKE (e.g. Orlanski and Sheldon, 1995). The BCEC takes place mostly in a layer between 300 and 10 Pa but extends below 500 Pa. The GFC precedes the development of strong BCEC, and the GFC maximum precedes the EKE maximum by about 0.5 Sol, similarly to that found by Ahmadi-Givi et al. (2014). The most negative BTEC (Fig. 15, contoured left column) is confined to above 300 Pa, which is expected as this is the height of the westerly jet. Once the BTEC fades away from near the system, the

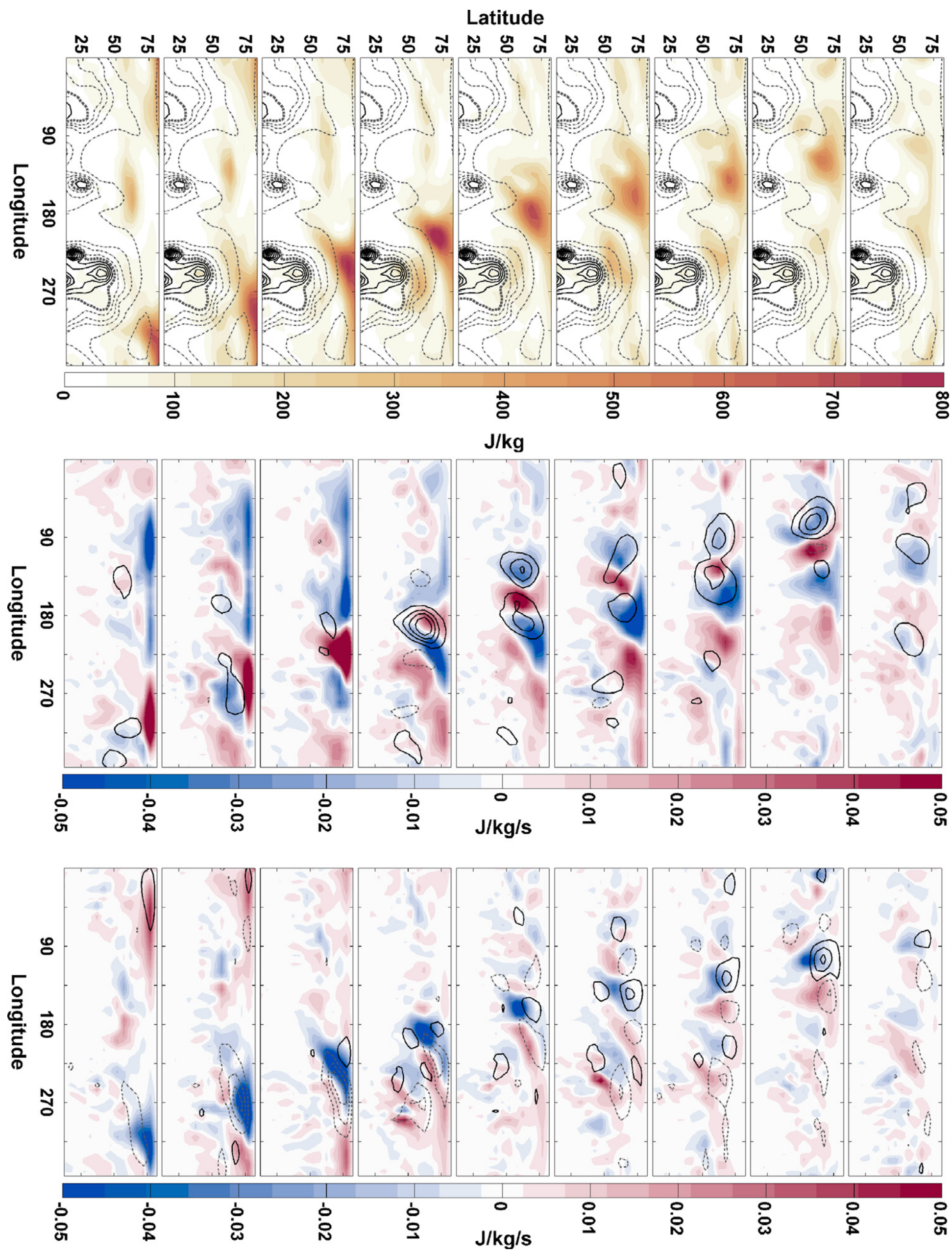

Fig. 16. Time series of vertical, pressure-weighted averages of eddy kinetic energy (left) with topography contoured as in Fig. 6, geopotential flux convergence (middle) with baroclinic energy conversion contoured at 0.008 J/kg/s increments and negative values dashed, and eddy kinetic energy transport (right) with barotropic energy conversion contoured at 0.008 J/kg/s increments and negative values dashed for a 4-Sol period traveling wave in MY 25 beginning at $L_s = 201.1^\circ$ and continuing at 0.33 Sol steps until $L_s = 202.7^\circ$.

geopotential flux convergence, which had been sustaining the system, switches to geopotential flux divergence as the wave continues to dissipate.

5.2. MY 25 example storm

We now contrast the MY 24 disturbance, which shows a similar structure to that of the storm in K13 and to terrestrial waves, to a local storm during the GDS of MY 25. The disturbance examined below is similar in form and duration to several other systems in MY 25 including a storm from $L_s = 211–214^\circ$, another $L_s = 218–221^\circ$, and several other weaker systems. An area of EKE is initiated in the same region as in the MY 24 case, northeast of Arabia Terra (Fig. 16, left column) at $L_s = 201.1^\circ$. The EKE maximum propagates eastward at approximately 80° Sol^{-1} (note each panel advances at 0.33 Sol). The wave then dissipates after $L_s = 202.7^\circ$ just west of Arabia Terra.

The GFC and EKE transport terms exhibit similar shapes and magnitudes relative to the EKE maximum as the MY 24 storm. GFC (Fig. 16, middle column) precedes any BCEC or BTEC. Once the wave packet is initiated, the GFC grows in concert with the EKE, and additional couplets develop upstream and downstream of the main GFC couplet. As in MY 24, the transport term (Fig. 16, right column) serves mostly as a local sink of EKE in the main area of EKE with a maximum directly downstream.

The primary differences between the MY 25 and MY 24 waves are the growth and decay mechanisms. The BCEC plays a lesser role in the strengthening of the EKE in MY 25 (Fig. 16, contoured middle column), though there are weak areas of BCEC throughout the growth of the wave. The BCEC only becomes a factor well into

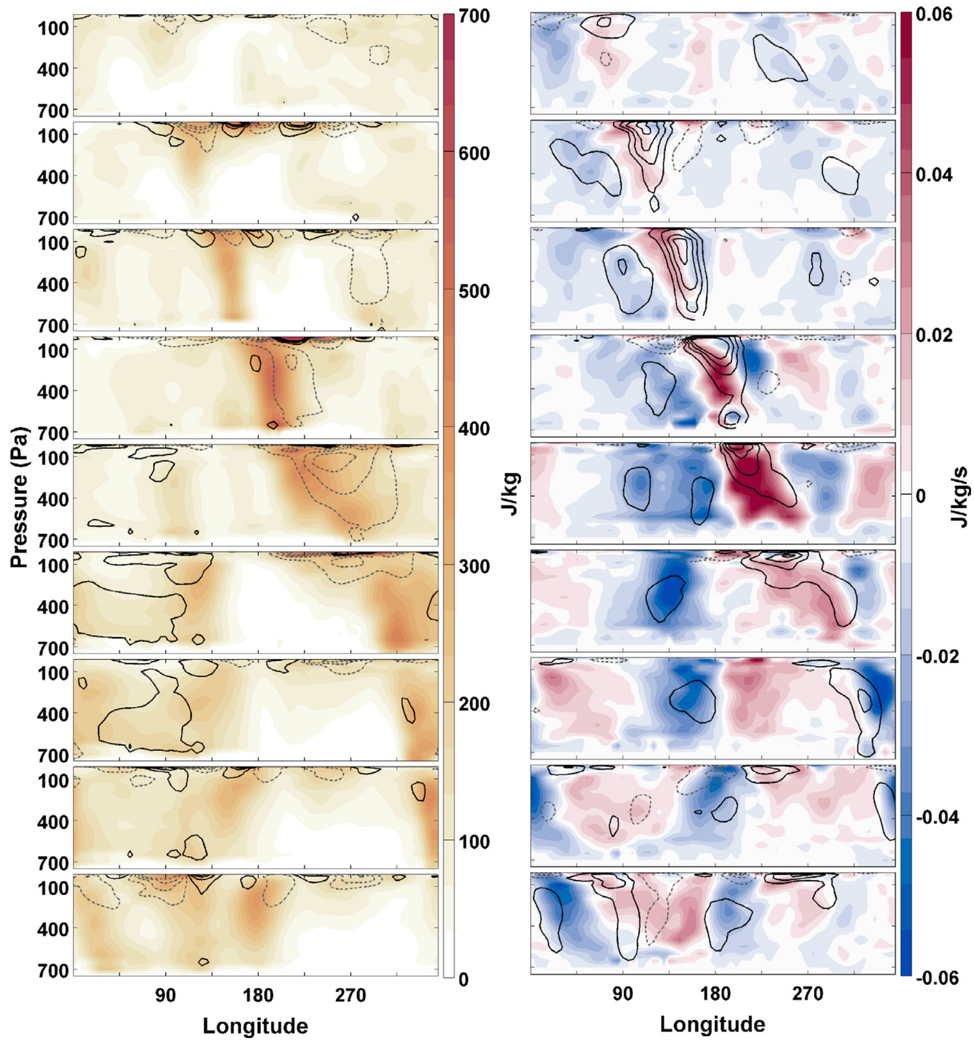

Fig. 17. Time series of the meridional average of eddy kinetic energy (left) with barotropic energy conversion contoured in 0.006 J/kg/s increments and negative values dashed and geopotential flux convergence (right) with baroclinic energy conversion contoured in 0.006 J/kg/s increments and negative values dashed in the 57.5–82.5°N latitude band for the wave in Fig. 16.

the development of the storm (sixth panel from top). This is unsurprising, as temperatures aloft are much warmer even at the beginning of the study period in MY 25 (Fig. 2), which has the effect of suppressing baroclinic instability by increasing static stability. Despite the reduced BCEC, the EKE attains a similar maximum magnitude as in the MY 24 storm. The reason for this is BTEC (Fig. 16, contoured right column), which unlike the MY 24 case, is positive during the development of the EKE packet. The EKE attains a magnitude similar to that for the MY 24 case, because the level of EKE depends on the difference between BCEC and BTEC rather than the magnitudes of each term (Simmons and Hoskins, 1980). However, BTEC does become a sink of EKE once the EKE packet reaches the Tharsis Plateau as in the MY 24 case. This pattern of weaker BCEC compensated by positive BTEC during development is a characteristic of storms in the GDS year.

The EKE has a deeper vertical structure in the MY 25 case than in the MY 24 case (Fig. 17, left column). A positive, amplifying pattern of EKE descends from 30 Pa at the second time step to 300 Pa at the sixth time step, which coincides with the one BCEC maximum (Fig. 17, contoured right column). The GFC (Fig. 17, right column) exhibits less tilt with height, a consequence of the reduced baroclinicity, and step seven shows an easterly tilt with height just before the barotropic decay begins. Also strong geopotential flux divergence remains throughout the existence of the eddy, unlike the MY 24 case where divergence only occurred once the eddy began to decay. The BTEC (Fig. 17, contoured left column) corroborates the finding above that the wave is a mixed barotropic/baroclinic wave; that is, the wave grows by both barotropic and baroclinic energy conversion. A tongue of positive BTEC grows from near 10 Pa to 400 Pa during the growth phase of the eddy. As the wave progresses, a downstream region of negative BTEC then takes over to hasten the decay of the wave

6. Intensities

The global-scale dust storm has a profound effect on the amount of EKE generated by the baroclinic waves. Fig. 18 shows the volume-integrated EKE and its generation terms for each MY in the 22.5–82.5°N band. MY 24 (blue) and MY 26 (green) maintain higher background levels of EKE throughout the L_s = 200–230° period than MY 25 (red). However, MY 26 does show reduced EKE similar to MY 25 after L_s = 220°. Though the background levels are reduced in MY 25, the maximum intensity of the storms is not diminished. The number of strong EKE generation events is reduced instead so that the EKE is generated in short bursts in MY 25. Three major events are clear: L_s = 201–203°, L_s = 214°, and L_s = 227–228° with other smaller events. This is contrasted to the two other years that have a higher background EKE level

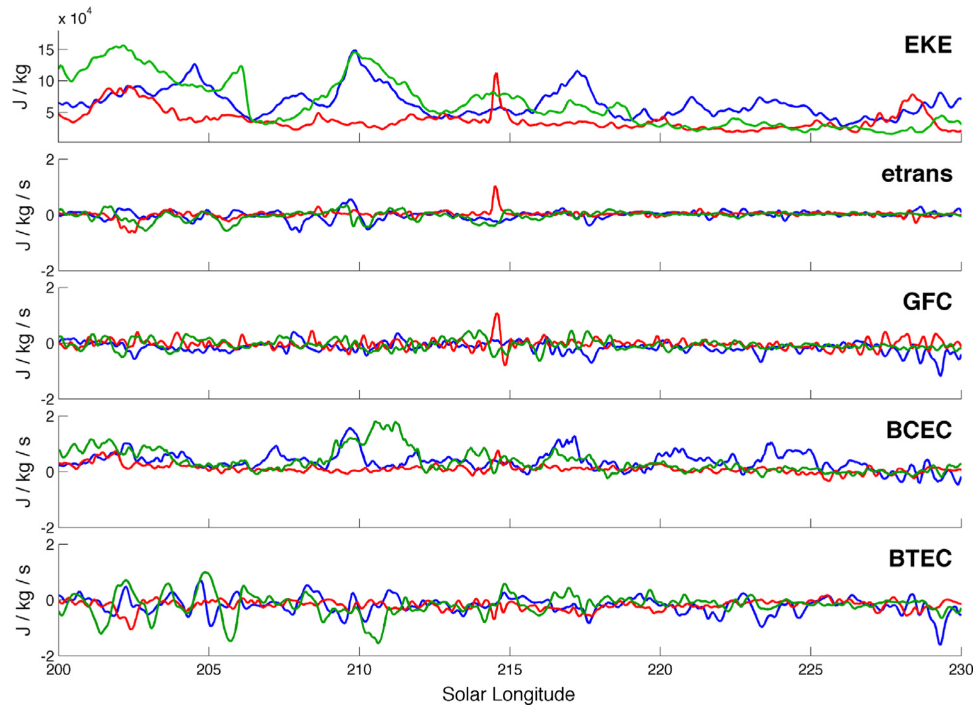

Fig. 18. Time series of the volume integrated EKE and EKE equation terms for the 22.5–82.5°N latitude band for MY 24 (blue), MY 25 (red), and MY 26 (green). (For interpretation of the references to color in this figure legend, the reader is referred to the web version of this article.)

with more frequently repeating EKE events. A qualitative counting of large EKE events in each year shows three large events in MY 25 and six events each in MY 24 and 26. Thus, the frequency of large EKE events is roughly halved in MY 25. A power spectrum (not shown) of the pressure-averaged EKE time series shows a peak at frequencies of five and six for MY 24 and 26 and a dominant peak at three for MY 25.

The MY 25, $L_s = 214^\circ$ event is unusual. The EKE spikes sharply and then falls to its background level equally as quickly. Concurrent spikes are recognized in the transport, BCEC, GFC, and BTEC terms. This storm defied analysis as the associated residue (not pictured) was larger than sum of the energy conversion and transport terms, and the EKE appeared to spontaneously develop across a large latitudinal and longitudinal swath simultaneously (30–70°N and 180–270°E). The timing of the system does not fall in a gap of TES retrievals, but retrievals are unavailable north of 30°N (Montabone et al., 2014, Fig. 2). In an attempt to explain this storm, the aforementioned analysis was duplicated on a beta-version of the EMARS reanalysis (Greybush et al., 2012). This particular storm was not present in the EMARS reanalysis. Thus, the MY 25, $L_s = 214^\circ$ storm may be an artifact of the MACDA reanalysis as a result of the bias encountered in the MY 25 GDS found in Montabone et al. (2006).

The two transport terms remain close to zero at almost all times for all three years. This is expected as the transport and GFC terms only move EKE and cannot be ultimate sources or sinks. Integrating the plots of Fig. 18 across time gives values of GFC and direct transport one to two orders of magnitude smaller than that of the energy conversion terms.

The BCEC term is nearly always positive for all three years but never climbs above 0.75 J/kg/s during MY 25. Conversely, MY 24 and 26 show periodic BCEC events with the volume integrated BCEC correlated to the volume integrated EKE at 0.67, 0.51, and 0.77 for years 24, 25, and 26, respectively, at a zero time-step lag. Also note that in all years near $L_s = 230^\circ$, BCEC is reduced compared to $L_s = 200^\circ$, reflective of the reverse of the tilt of the polar front between the two time periods and decrease in meridional temperature gradient, stabilizing the atmosphere to baroclinic instability (see Fig. 2). The BTEC experiences similar values and fluctuations from the mean for each year. Average values are negative but occasionally become positive during large EKE generation events. During MY 25, the BTEC experiences a reduced number of positive events and is closer to zero on average. The reduced magnitude of BTEC is attributable to two causes. One, a sink of EKE will be smaller if there is less EKE generated, and two, the relative higher average of BTEC during MY 25 is due these periodic areas of positive BTEC during transient waves being averaged into the volume integrated total at each time step.

7. Conclusions

The dynamics and energetics of transient waves during the late fall season in the northern hemisphere of the atmosphere of Mars were investigated during three Mars years. MACDA provided the reanalysis data for the comparison of two years without global-scale dust storms (MY 24 and MY 26) to a year with a global-scale dust storm (MY 25). The eddy kinetic energy equation was the primary tool used for the analysis of the data. In comparing the three years, the following conclusions can be drawn:

The waves of the clear years of MY 24 and MY 26 show eddy kinetic energy growth and decay mechanisms similar to those that were described by Kavulich et al. (2013). Below 10 Pa, waves generate eddy kinetic energy primarily by baroclinic energy conversion. Barotropic energy conversion acts mostly as a sink of eddy kinetic energy downstream of the main regions of baroclinic energy conversion, though it can act as a source of eddy kinetic energy directly west of the Tharsis Plateau, extending the storm track downstream of the main baroclinic energy conversion regions. Geopotential flux convergence provides the triggering mechanism for wave development and baroclinic energy conversion and also plays a role in the decay of waves.

In the global-scale dust storm year of MY 25, the intensity of baroclinic energy conversion is substantially reduced due to decreased vertical wind shear between 500 and 800 Pa. Further inhibition of eddy heat fluxes results from the more isothermal, statically stable atmosphere above 500 Pa. This leads to a weaker sensitivity of the atmosphere to baroclinic instability. This weaker sensitivity reduces the frequency of storms to roughly half of that during non-dust-storm years. However, compared to MY 24 and 26, the absolute intensity of the individual eddy kinetic energy generation events does not decrease. The storms during MY 25 become mixed baroclinic/barotropic: the waves gain energy both baroclinically and barotropically and lose it barotropically. Once the wave begins to lose energy barotropically, it begins to generate energy baroclinically, which compensates for the loss of EKE due to BTEC.

Future research plans include an extension of the study period to include the second maximum in wave activity during the late winter period, a comparison of the energetics of high eddy activity periods to that of the solsticial pause, and an expansion of these analyses to the southern hemisphere. Moreover, we hope to duplicate the analysis found here to additional reanalysis datasets as they become available.

Acknowledgments

The authors thank Drs. Luca Montabone, Stephen Lewis, and Peter Read for making the MACDA dataset publicly available and Dr. Steve Greybush and John Wilson for access to early, beta versions of the EMARS dataset. The reviewers, Dr. Luca Montabone and Dr. David Mulholland, provided many helpful comments that improved the quality of this work. This work fulfills part of the Ph.D. requirements of the first author.

References

Ahmadi-Givi, F., Nasr-Esfahany, M., Mohebalhojeh, A.R., 2014. Interaction of North Atlantic baroclinic wave packets and the mediterranean storm track. Q. J. R. Meteorol. Soc. 140 (680), 754–765. doi:10.1002/qj.2171.

Banfield, D., Conrath, B., Gierasch, P., et al., 2004. Traveling waves in the martian atmosphere from MGS TES Nadir data. Icarus 170 (2), 365–403. doi:10.1016/j.icarus.2004.03.015.

Banfield, D., Conrath, B., Smith, M., et al., 2003. Forced waves in the martian atmosphere from MGS TES Nadir data. Icarus 161 (2), 319–345. doi:10.1016/S0019-1035(02)00044-1.

Barnes, J.R., 1980. Time spectral analysis of midlatitude disturbances in the martian atmosphere. J. Atmos. Sci. 37 (9), 2002–2015.

Barnes, J.R., 1981. Midlatitude disturbances in the martian atmosphere: A second Mars year. J. Atmos. Sci. 38 (2), 225–234.

Barnes, J.R., 1984. Linear baroclinic instability in the martian atmosphere. J. Atmos. Sci. 41 (9), 1536–1550. doi:10.1175/1520-0469(1984)041⟨1536:LBIITM⟩2.0.CO;2.

Barnes, J.R., Pollack, J.B., Haberle, R.M., et al., 1993. Mars atmospheric dynamics as simulated by the NASA Ames general circulation. J. Geophys. Res. 98 (E2), 3125–3148.

Basu, S., Wilson, J., Richardson, M., et al., 2006. Simulation of spontaneous and variable global dust storms with the GFDL Mars GCM. J. Geophys.Res. 111 (E9), E09004. doi:10.1029/2005JE002660.

Blumsack, S.L., Gierasch, P.J., 1972. Mars: The effects of topography on baroclinic instability. J. Atmos. Sci. 29 (9), 1081–1089.

Cantor, B.A., 2007. MOC observations of the 2001 Mars planet-encircling dust storm. Icarus 186 (1), 60–96. doi:10.1016/j.icarus.2006.08.019.

Cantor, B.A., James, P.B., Caplinger, M., et al., 2001. Martian dust storms: 1999 Mars orbiter camera observations. J. Geophys. Res. 106 (E10), 23653–23687.

Chang, E.K.M., 1993. Downstream development of baroclinic waves as inferred from regression analysis. J. Atmos. Sci. 50 (13), 2038–2053.

Chang, E.K.M., 2000. Wave packets and life cycles of troughs in the upper troposphere: Examples from the southern hemisphere summer season of 1984/85. Mon. Weather Rev. 128 (1), 25–50. doi:10.1175/1520-0493(2000)128⟨0025:WPALCO⟩2.0.CO;2.

Chang, E.K.M., Orlanski, I., 1993. On the dynamics of storm track. J. Atmos. Sci. 50 (7), 999–1015.

Chang, E.K.M., Orlanski, I., 1994. On energy flux and group velocity of waves in baroclinic flows. J. Atmos. Sci. 51 (24), 3823–3828.

Charney, J.G., 1947. The dynamics of long waves in a baroclinic westerly current. J.Meteorol. 4 (5), 135–162.

Collins, M., Lewis, S.R., Read, P.L., 1996. Baroclinic wave transitions in the martian atmosphere. Icarus 136 (120), 344–357.

Conrath, B.J., 1975. Thermal structure of the martian atmosphere during the dissipation of the dust storm of 1971. Icarus 24 (1), 36–46. doi:10.1016/0019-1035(75)90156-6.

Decker, S.G., Martin, J.E., 2005. A local energetics analysis of the life cycle differences between consecutive, explosively deepening, continental cyclones. Mon. Weather Rev. 133 (1), 295–316.

Eady, B.E.T., 1949. Long waves and cyclone waves. Tellus 1 (3), 33–52.

Forget, F., Hourdin, F., Fournier, R., et al., 1999. Improved general circulation models of the martian atmosphere from the surface to above 80 km. J. Geophys. Res. 104 (E10), 24155. doi:10.1029/1999JE001025.

Greybush, S.J., Kalnay, E., Hoffman, M.J., et al., 2013. Identifying martian atmospheric instabilities and their physical origins using Bred vectors. Q. J. R. Meteorol. Soc. 139 (672), 639–653. doi:10.1002/qj.1990.

Greybush, S.J., Wilson, R.J., Hoffman, R.N., et al., 2012. Ensemble Kalman filter data assimilation of thermal emission spectrometer temperature retrievals into a Mars GCM. J. Geophys. Res. 117 (E11), E11008. doi:10.1029/2012JE004097.

Haberle, R.M., Pollack, J.B., Barnes, J.R., et al., 1993. Mars atmospheric dynamics as simulated by the NASA Ames general circulation model 1. The zonal-mean circulation. J. Geophys. Res. 98, 3093–3124.

Hinson, D.P., Wang, H., 2010. Further observations of regional dust storms and baroclinic eddies in the northern hemisphere of Mars. Icarus 206 (1), 290–305. doi:10.1016/j.icarus.2009.08.019.

Hinson, D.P., Wilson, R.J., 2002. Transient eddies in the southern hemisphere of Mars. Geophys. Res. Lett. 29 (7), 3–6. doi:10.1029/2001GL014103.

Hollingsworth, J.L., Barnes, J.R., 1996. Forced stationary planetary waves in Mars's winter atmosphere. J. Atmos. Sci. 53 (3), 428–448.

Hollingsworth, J.L., Haberle, R.M., Barnes, J.R., et al., 1996. Orographic control of storm zones on Mars. Nature 380, 413–416.

Hoskins, B.J., Valdes, P.J., 1990. On the existence of storm-tracks. J. Atmos. Sci. 47 (15), 1854–1864.

Hurley, J., Teanby, N., Irwin, P., et al., 2014. Differentiability and retrievability of CO_2 and H_2O clouds on Mars from MRO/MCS measurements: A radiative-transfer study. Planet. Space Sci. 97, 65–84. doi:10.1016/j.pss.2014.03.015.

Kavulich, M.J., Szunyogh, I., Gyarmati, G., et al., 2013. Local dynamics of baroclinic waves in the martian atmosphere. J. Atmos. Sci. 70 (11), 3415–3447. doi:10.1175/JAS-D-12-0262.1.

Kuroda, T., Medvedev, A.S., Hartogh, P., et al., 2007. Seasonal changes of the baroclinic wave activity in the northern hemisphere of Mars simulated with a GCM. Geophys. Res. Lett. 34 (9), L09203. doi:10.1029/2006GL028816.

Leovy, C.B., 1969. Mars: Theoretical aspects of meteorology.. Appl. Opt. 8 (7), 1279–1286.

Lewis, S.R., Mulholland, D.P., Read, P.L., et al., 2016. The solsticial pause on Mars: 1 A planetary wave reanalysis. Icarus 264, 456–464. doi:10.1016/j.icarus.2015.08.039.

Lewis, S.R., Read, P.L., Conrath, B.J., et al., 2007. Assimilation of thermal emission spectrometer atmospheric data during the Mars Global Surveyor aerobraking period. Icarus 192 (2), 327–347. doi:10.1016/j.icarus.2007.08.009.

Lovejoy, S., Muller, J.-P., Boisvert, J.P., 2014. On Mars too expect macroweather. Geophys. Res. Lett. 41, 7694–7700. doi:10.1002/2014GL061861, Received.

Mitchell, D.M., Montabone, L., Thomson, S., et al., 2014. Polar vortices on Earth and Mars: A comparative study of the climatology and variability from reanalyses. Q. J. R. Meteorol. Soc. 141 (687), 550–562. doi:10.1002/qj.2376.

Montabone, L., Lewis, S.R., Read, P.L., 2005. Interannual variability of martian dust storms in assimilation of several years of Mars global surveyor observations. Adv. Space Res. 36 (11), 2146–2155. doi:10.1016/j.asr.2005.07.047.

Montabone, L., Lewis, S.R., Read, P.L., et al., 2006. Validation of martian meteorological data assimilation for MGS/TES using radio occultation measurements. Icarus 185 (1), 113–132. doi:10.1016/j.icarus.2006.07.012.

Montabone, L., Marsh, K., Lewis, S.R., et al., 2014. The Mars analysis correction data assimilation (MACDA) dataset V1.0. Geosci. Data J. 1, 129–139. doi:10.1002/gdj3.13.

Mooring, T.A., Wilson, R.J., 2015. Transient eddies in the MACDA Mars reanalysis. J. Geophys. Res.: Planets 120, 1–26. doi:10.1002/2015JE004824.

Mulholland, D.P., Lewis, S.R., Read, P.L., et al., 2016. The solsticial pauseon Mars: 2 modelling and investigation of causes. Icarus 264, 465–477. doi:10.1016/j.icarus.2015.08.038.

Murphy, R., Pollack, B., Haberle, M., et al., 1995. Three-dimensional numerical simulation of martian global dust storms. J. Geophys. Res.: Planets 100 (E12), 26357–26376.

O'Brien, J., 1970. Alternative solutions to the classical vertical velocity problem. J. Appl. Meteorol. 9 (2), 197–203.

Orlanski, I., Chang, E.K.M., 1993. Ageostrophic geopotential fluxes in downstream and upstream development of baroclinic waves. J. Atmos. Sci. 50 (2), 212–225.

Orlanski, I., Katzfey, J., 1991. The life cycle of a cyclone wave in the southern hemisphere. Part I: Eddy energy budget. J. Atmos. Sci. 48 (17), 1973–1998.

Orlanski, I., Sheldon, J.P., 1993. A case of downstream baroclinic development over Western North America. Mon. Weather Rev. 121 (11), 2929–2950.

Orlanski, I., Sheldon, J.P., 1995. Stages in the energetics of baroclinic systems. Tellus A 47 (5), 605–628.

Pollack, J.B., Leovy, C.B., Grieman, P.W., et al., 1981. A martian general circulation experiment with large topography. J. Atmos. Sci. 38 (1), 3–29. doi:10.1175/1520-0469(1981)038⟨0003:AMGCEW⟩2.0.CO;2.

Simmons, A.J., Hoskins, B., 1979. The downstream and upstream development of unstable baroclinic waves. J. Atmos. Sci. 36 (7), 1239–1254.

Simmons, A.J., Hoskins, B.J., 1978. The life cycles of some nonlinear baroclinic waves. J. Atmos. Sci. 35 (3), 414–432. doi:10.1175/1520-0469(1978)035⟨0414:TLCOSN⟩2.0.CO;2.

Simmons, A.J., Hoskins, B.J., 1980. Barotropic influences on the growth and decay of nonlinear baroclinic waves. J. Atmos. Sci. 37 (8), 1679–1984.

Smith, M., 2002. Thermal emission spectrometer observations of martian planet-encircling dust storm 2001A. Icarus 157 (1), 259–263. doi:10.1006/icar.2001.6797.

Strausberg, M.J., 2005. Observations of the initiation and evolution of the 2001 Mars global dust storm. J. Geophys. Res. 110 (E2), E02006. doi:10.1029/2004JE002361.
Swanson, K., Pierrehumbert, R.T., 1994. Nonlinear wave packet evolution on a baroclinically unstable jet. J. Atmos. Sci. 51 (3), 384–396.
Tabataba-vakili, F., Read, P.L., Lewis, S.R., et al., 2015. A Lorenz/Boer energy budget for the atmosphere of Mars from a reanalysis of spacecraft observations. Geophys. Res. Lett. 42, 8320–8327. doi:10.1002/2015GL065659.
Wang, H., Richardson, M.I., 2015. The origin, evolution, and trajectory of large dust storms on Mars during Mars years 2430 (19992011). Icarus 251, 112–127. doi:10.1016/j.icarus.2013.10.033.
Wang, H., Zurek, R.W., Richardson, M.I., 2005. Relationship between frontal dust storms and transient eddy activity in the northern hemisphere of Mars as observed by Mars Global Surveyor. J. Geophys. Res. 110 (E7), E07005. doi:10.1029/2005JE002423.
Wang, P., Mitchell, J.L., 2014. Planetary ageostrophic instability leads to superrotation. Geophys. Res. Lett. 41 (12), 4118–4126. doi:10.1002/2014GL060345.
Wilson, R.J., Banfield, D., Conrath, B.J., et al., 2002. Traveling waves in the Northern Hemisphere of Mars. Geophys. Res. Lett. 29 (14), 3–6. doi:10.1029/2002GL014866.